ISSN: 2164-5388 Volume 9, Number 2, April 2019

Scientific Research Publishing

Open Journal of Biophysics

ISSN: 2164-5388

www.scirp.org/journal/ojbiphy

Journal Editorial Board

ISSN Print: 2164-5388 ISSN Online: 2164-5396
http://www.scirp.org/journal/ojbiphy

Associate Editors

Editorial Board

Scientific Research Publishing

Open Journal of Biophysics, 2019, 9, 83-145
http://www.scirp.org/journal/ojbiphy
ISSN Online: 2164-5396
ISSN Print: 2164-5388

Table of Contents

Volume 9 Number 2 April 2019

Open Journal of Biophysics (OJBIPHY)
Journal Information

SUBSCRIPTIONS

The *Open Journal of Biophysics* (Online at Scientific Research Publishing, www.SciRP.org) is published quarterly by Scientific Research Publishing, Inc., USA.

Subscription rates:
Print: $79 per issue.
To subscribe, please contact Journals Subscriptions Department, E-mail: sub@scirp.org

SERVICES

Advertisements
Advertisement Sales Department, E-mail: service@scirp.org

Reprints (minimum quantity 100 copies)
Reprints Co-ordinator, Scientific Research Publishing, Inc., USA.
E-mail: sub@scirp.org

COPYRIGHT

PRODUCTION INFORMATION

For manuscripts that have been accepted for publication, please contact:
E-mail: ojbiphy@scirp.org

Scientific Research Publishing

Open Journal of Biophysics, 2019, 9, 83-87
http://www.scirp.org/journal/ojbiphy
ISSN Online: 2164-5396
ISSN Print: 2164-5388

Mimicking Bone Chemical Composition Using Economical Materials for X-Ray Imaging Quality Assurance and Educational Purposes

Shyma M. Alkhateeb

Diagnostic Radiography Technology Department, Faculty of Applied Medical Sciences, King Abdulaziz University, Jeddah, KSA
Email: smalkhateeb@kau.edu.sa

How to cite this paper: Alkhateeb, S.M. (2019) Mimicking Bone Chemical Composition Using Economical Materials for X-Ray Imaging Quality Assurance and Educational Purposes. *Open Journal of Biophysics*, **9**, 83-87.
https://doi.org/10.4236/ojbiphy.2019.92006

Received: January 22, 2019
Accepted: February 22, 2019
Published: February 25, 2019

Abstract

Imaging different bone sites for medical education requires the formation of bone-equivalent materials that mimic bone density. We investigated an economic imaging composition that characterizes bone density in imaging for quality assurance and educational purposes. Four different compositions were tested to reveal the best composition in simulating bone density in X-ray imaging. Hydrated lime was discovered to be the most suitable because it is durable (stiff and does not crumble), easy to source and process, and attenuates imaging X-rays enough to resemble real bone. Hydrated lime provides a significantly better phantom than the other combinations used.

Keywords

Bone, Phantom, Quality Assurance, Education, Hydrated Lime

1. Introduction

Radiologic anatomical phantoms are commercially available for quality assurance and educational purposes. However, these phantoms are considered expensive and do not demonstrate all pathological complications. Therefore, materials that can convincingly simulate bone in X-ray imaging, for educational and quality-assurance purposes, have generated great interest.

Bone is composed of organic and inorganic compounds in the form of minerals. Living bone consists of 10% - 20% water and 60% - 70% minerals, with most of the rest comprising collagen and small amounts of other substances, such as proteins and inorganic salts [1]. Organic components, mostly collagen, represent 33% of total bone composition. Inorganic components consist of calcium (39%),

phosphate (17%), carbonate (9.8%), sodium (0.7%) and magnesium (0.5%) [2].

The mineral component can be approximated by hydroxyapatite (HA, $Ca_{10}(PO_4)_6(OH)_2$). Since the composition of real bone minerals is much more complex, and contains supplementary ions such as silicon and zinc, bone minerals have Ca:P ratios ranging from 1.37 - 1.87 [1]. Jastaniah (2016) produced a mixture of materials that contained egg shells and cement to reproduce bones in X-ray imaging [3]. Although egg shell is an environmentally friendly and economical substance, it is difficult to collect, maintain hygienically, and process.

The aim of this research was to mimic bone-chemical composition for X-ray imaging, by constructing an economical phantom with widely available materials, whose density closely matched that of bone. Materials closely resembling the mineral ingredients of bone, calcium (mainly), and collagen were used to construct the phantom. The resulting product of these constituents can simulate bone in different anatomical and pathological conditions, for both quality assurance and educational purposes.

2. Materials and Methods

Materials of a similar density to that of bone were chosen for X-ray imaging. Hydrated lime (calcium hydroxide $Ca(OH)_2$) was used to represent calcium [4]. Since the molecular compositions of collagen and gelatin are almost identical [5], agar gelatin, an environmentally friendly and economical substance, was used to represent collagen. Agar is extracted from red seaweed (Rhodophyceae) and was discovered in Japan in the mid-seventeenth century and introduced to the west in 1859. Agarose, the structural unit of agar, is a linear polymer composed of (1-3)-linked agarobiose units of β-d-galactopyranose (1-4)-linked to 3,6-anhydro-α-l-galactopyranose [6]. Potassium phosphatewas also used in the construction of the phantoms, representing the phosphate content in bone.

Four samples of different proportions of various components were prepared to investigate the chemical composition that best mimicked bone in X-ray imaging (see **Table 1**).

Hydrated lime is a building substance, purchased from a building materials store and manufactured by Arabian Industries, Riyadh, Kingdom of Saudi Arabia. Agar strips, originating from China, were purchased from a grocery store. The agar was ground to a powder, the lime was filtered, and all solid materials were blended together. The mixing process of four (10 cm-wide) shakes per second for 1 minute mixed all solid materials homogeneously. These materials were mixed with Safa (branded) water (Ca-Na-HCO_3-C1-SO_4) [7]. The major ion concentrations and physical properties of the water (as indicated by the manufacturer) are illustrated in **Table 2**. One ppm is equivalent to one milligram of ions per liter of water (mg/L).

All solid mixtures (**Table 1**) were mixed with half the amount of water. For example, if 100 g of material constituted the solid part of the sample, 50 mL of water constituted the remainder. Due to their relatively negligible concentrations,

Table 1. Four samples of different proportions of various components.

Sample number	Chemical composition of solid materials
1	100% lime
2	70% lime, 30% gelatin
3	40% lime, 30% gelatin, 30% KPO
4	70% lime, 30% KPO

Table 2. Major ion concentrations of Safa water, as indicated by the manufacturer, in parts per million (ppm) [7].

Ca	Mg	Na	K	Fe	HCO_3	SO_4	NO_3	Cl	F	BrO_3
19.0	3.0	19.0	1.80	0.00	39.0	27.0	2.80	33.0	1.00	<0.01

the ions present in the water before mixing were ignored. For example, the weight of sodium ions (Na = 19 ppm) in 1 mL of water is only 0.0190 mg, which is relatively insignificant. Mixtures were cast in molds to mirror bone dimensions. The X-ray machine used to image the samples was a Definium 6000, General Electric, 2009 with imaging parameters set as 10 mA, 50 kV, and 1.6 mAs.

3. Results and Discussion

The four samples, listed in Table 1, were formed and imaged together with shoulder bones detached from a real demonstration skeleton (Figure 1). This arrangement allowed the bones to act as a control.

The choice of ideal sample depended on the qualitative information gathered in Table 3. Durability of the samples means their ability to be re-used and stand-alone without crumbling. X-ray image acceptance of different samples compared to the real clavicle bone was obtained from highly experienced radiography personnel.

Sample one was clearly the best material and met all our specifications (Table 3). Despite sample two lacking durability (crumbling), it was the next best. Both samples three and four X-ray images were not acceptable because of the inhomogeneity that can be presented in their structure. The raw materials for samples one and two are easy to find and process. Therefore, two additional samples comprising the same materials in the same proportions as samples one and two, but of different sizes, were prepared. The additional samples were made in cylindrical-shaped molds of 2 cm diameter and 1 cm and 2 cm thickness. A radiograph of both samples, with a clavicle bone as a control, was obtained to examine X-ray intensity (see Figure 2).

Figure 2 shows the intensity match of different bone thicknesses with different thicknesses in sample one. Sample two has a higher absorption of X-rays for both thicknesses compared to bone. The difference in intensity seen in the middle of sample 1, with 1 cm thickness, reflects a change of 2 mm in thickness.

Figure 1. Radiograph of the four samples (Table 1) with the shoulder-bone controls.

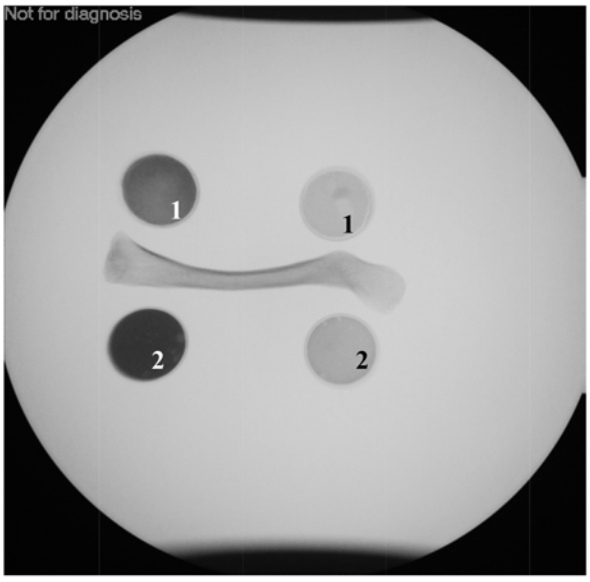

Figure 2. Radiograph of samples 1 and 2 with 1 cm (light) and 2 cm (dark) thicknesses, with a clavicle as control.

Table 3. Material choice characteristics.

Sample number	Sample characterization			
	Easy to find materials	Easy to produce	Durability	X-ray image acceptance
1	Yes	Yes	Yes	Yes
2	Yes	Yes	No	Yes
3	No	No	No	No
4	No	Yes	No	No

4. Conclusion and Recommendations

The idea of discovering a new economical material that mimics bone density in X-ray imaging started when trying to make phantoms of different bone fractures and sites for medical education and quality assurance purposes. Different materials have been discovered in the literature, however, they are not economical, durable, nor easy to produce. Among the tested materials in this study, the most economical at mimicking bone in X-ray imaging was hydrated lime. Hydrated lime is durable (stiff and does not crumble), easy to find and process, and has a good X-ray image intensity compared with that of real bone. Future work should involve X-ray imaging testing of different hydrated-lime morphologies that simulate their real-bone counterparts.

Acknowledgements

All thanks to The Creator for His blessings. I would like to thank radiographers Mr. Shuraim Alyami and Mr. Hashim Alalawi for operating the X-ray machine, acquiring the radiographs, and optimizing the images. Special thanks to Dr. Saddig Jastaniah for qualifying the resultant images. I would also like to thank Editage (http://www.editage.com/) for English language editing.

Conflicts of Interest

The author declares no conflicts of interest regarding the publication of this paper.

References

[1] Cambridge, U.O. (2011) Structure and Composition of Bone. Structure of Bone and Implant Materials. https://www.doitpoms.ac.uk/tlplib/bones/structure.php

[2] Martini, F.H., Nath, J.L. and Bartholomew, E.F. (2012) Fundamentals of Anatomy and Physiology. 11 Edition, Pearson Education, Inc., London, England.

[3] Jastaniah, S.D. (2016) Novel Mixture of Materials Produces Bone- and Soft Tissue-Like Imaging Density. *Open Journal of Biophysics*, **6**, 90-97. https://doi.org/10.4236/ojbiphy.2016.64010

[4] Herrin, M. and Mitchell, H. (1961) Lime-Soil Mixtures. In 40*th Annual Meeting of the Highway Research Board*, Highway Research Board.

[5] Djabourov, M., Lechaire, J.-P. and Gaill, F. (1993) Structure and Rheology of Gelatin and Collagen Gels. *Biorheology*, **30**, 191-205. https://doi.org/10.3233/BIR-1993-303-405

[6] Imeson, A. (2009) Agar, in Food Stabilisers, Thickeners and Gelling Agents. Wiley Online Library, Hoboken. https://doi.org/10.1002/9781444314724.ch3

[7] Al-Zahrani, F.S.A., Albaqshi, H.A.A., Alhelal, G.A.M., *et al.* (2017) Bottled Water Quality in KSA. *IJISET-International Journal of Innovative Science, Engineering & Technology*, **4**, 2348-7968.

Scientific Research Publishing

Open Journal of Biophysics, 2019, 9, 88-97
http://www.scirp.org/journal/ojbiphy
ISSN Online: 2164-5396
ISSN Print: 2164-5388

Determination of the Optical Properties of Basal Cancer Using OCT System

Sohad Elwakeel[1*], Nafie Almuslet[1], Yahia Badr Aldeen[2], Khalid Haroun[3]

[1]Institute of Laser, Sudan University of Science and Technology, Khartoum, Sudan
[2]National Institute of Laser Enhanced Science, Cairo University, Cairo, Egypt
[3]Facility of Radiobiological and Imagine Science, Alzaaim Alazahari University, Khartoum, Sudan
Email: *sohadelwakeel@gmail.com, mnmfa2008@yahoo.com, ybeldeen @hotmail.com, khalmai@hotmail.com

How to cite this paper: Elwakeel, S., Almuslet, N., Aldeen, Y.B. and Haroun, K. (2019) Determination of the Optical Properties of Basal Cancer Using OCT System. *Open Journal of Biophysics*, **9**, 88-97.
https://doi.org/10.4236/ojbiphy.2019.92007

Received: December 30, 2018
Accepted: February 24, 2019
Published: February 27, 2019

Abstract

The objective of this work is to determinate the optical properties of basal cancer cells using an optical coherence tomography (OCT). OCT system with He-Ne & diode laser was used to make interference pattern for the basal cancer, then the output was displayed by optical detector, information of an electrical signal passed to the digital oscilloscope to give the object information after Fourier transform processing for that signal, then PC and CCD were used to display FFT signal. Finally many steps were done to determine the optical properties for the basal cancer. The intensity of the signals was plotted against scanning distance; the obtained graphs were used to determine the penetration depth and absorption coefficient.

Keywords

Optical Imaging, Resolution, FT, Cancer Cell, Optical Properties

1. Introduction

Skin cancer is the most common form of cancer [1]. Nonmelanoma skin cancers, including basal cell carcinomas (BCCs) and squamous cell carcinomas (SCCs), are more common than all other types of human cancers [2].

Basal cell carcinoma (BCC) is the most prevalent skin cancer among caucasians [3] [4]. BCCs are derived from keratinocytes [5]. The incidence of BCC continues to increase worldwide [6]. It is a multifactorial disease in which excessive sun exposure plays a major pathogenic role [7] [8]. Treatment strategy has changed in the last two decades [9]. Nowadays, a broad variety of imaging techniques are becoming available. Optical imaging, also known as optical tomography, has become an active research field [10]. Several optical imaging techniques

being investigated include time resolved-optical imaging, frequency-domain optical imaging, optical coherence tomography, optoacoustic tomography and ultrasound-modulated optical (acousto-optical) tomography [11].

Optical coherence tomography is a relatively new noninvasive [12] [13] [14] optical imaging modality for biomedical diagnosis. It is based on low coherence reflectometry which was first developed for telecommunication devices of a high precision in the range of micrometers and lateral introduce to biomedical areas as a method to map the contour and monitor the thickness of retina [15]. The use of optical techniques for diagnostic purpose relies on the capability to measure the optical properties of different tissues. In the fact, a degree of contrast must exist between absorption and scattering coefficients for effective detection of tissue alteration using optical imaging [16].

Recently, extensions of OCT technology, including Doppler flow and polarization sensitive image, have been developed that permit spatially resolved imaging of velocity or birefringence [17].

In ordinary diagnostic, and to understand the origins of disease, material to be examined must be excised from the body and brought to the microscope.

While OCT has potential to go inside the tissue and give us the information from the reflected light, OCT performs imaging by measuring the echo time delay and intensity of backscattered light from internal microstructure in the tissue [18].

The advantages of OCT, as compared to other imaging methods such as CT, NMR and ultrasonic, are that there is no ionizing radiation involved, the method is non invasive, and it is high precision, and lack of need for mechanical contact between instrument and eye, high depth. Doppler imaging is capable of simultaneous imaging and real-time flow measurements [19].

However, there is also a demand for gaining insight into functional parameters of tissue, such as the blood oxygen content. With OCT, we can diagnose small segments of tissue as opposed to most of other imaging modalities that can scan the whole organ; image can be acquired *in vivo* and in real time without loss of information for unknown sample structure [20]. In addition, it also precludes the need for surgical biopsies and hence avoids discomfort and bleeding of biopsies [21].

Because the velocity of light is extremely high, the echo time delay cannot be measured directly. Instead, it is necessary to use correlation or interferometery techniques [22].

In an OCT system the spectrum of the source is very important as it determines the maximum resolution of the image.

The general requirements of sources of OCT imaging are [23]:

1) Emission in near IR 2) Short coherence length 3) High irradiance

Since OCT has a much higher spatial resolution compared to other imaging modalities, the ability to image internal structures without the need for mechanical probing makes this technique very powerful for medical applications [24]. Its applications in ophthalmology, dermatology, endoscope, cardiology, vascular

morphology, gastroterology, dentistry, and embryology have been demonstrated by several groups [25]. In this study, optical properties of basal cancer were determined by OCT system.

2. Materials and Methods

Laser source (diode 1550) nm, ≤4.25 mW, class III) constructed Michelson interferometer, detector, digital oscilloscope (150 MHz), computer, printer, CCD (LBA-100A) camera.

In this study different cancer cells samples were investigated.

First, laser light incident on the beam splitter, which reflects half of the incident light to the reference mirror which was fixed, and the other half of the incident light was transmitted to the object (the basal cancer) through the concave lens. **Figure 1** shows the block diagram of the constructed system.

Then the two beams were reflected or backscattered again to the beam splitter, and interference fringes were obtained after some adjustment done by screws on the fixed mirror. This step was done for all the samples and to scan the sample depth, a micrometer screw was used.

The performed pattern was received by the detector to convert it into voltage, which was displayed on the digital oscilloscope.

Automatic calibration was used to get high accuracy for measurement. Vertical position axis was used to adjust the signal position in the screen, and to display all signals information "Math" button must be pushed, then advanced functions are displayed, and FT can be selected to allow acquired waveforms to be converted into frequency domain traces.

At the last, "Measure" button must be pressed and waveforms information are displayed.

The intensity of that signal was represented (plotted) against scanning distance; the obtained graph was used to determine penetration depth and absorption coefficient. From absorption coefficient all other optical properties can be calculated.

3. Results and Discution

The experimental results, which related to the investigation of different cancer samples, were represented in tables, figures and images. **Figures 2-5** show the signal recorded by digital oscilloscope.

Figure 2 shows the tissue signal, ones in the center of the figure represent signal before FT, while the lower ones after FT. Information's after FT are: frequency 1.111 kHz, peak 240 mv, width 0.6 ms, period 0.9 ms and SNR (backscattered power divided by the noise equivalent bandwidth of the detection) 20 dB.

Figure 3 shows the tissue signal, (a) in normal ordinate before FT, while (b) after FT. Information's displayed on digital oscilloscope for second (BCC) sample are frequency 833.3 Hz, peak 330 mv, width 0.5 ms, period 1.2 ms and SNR 20 dB.

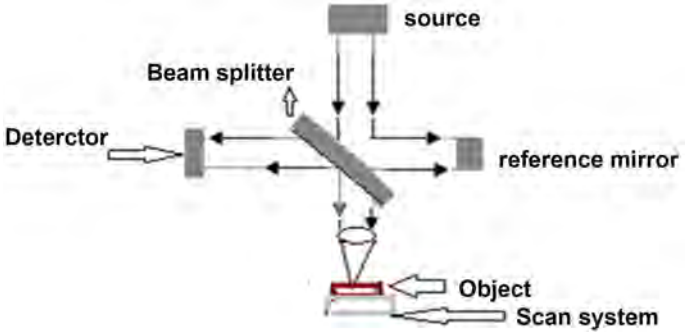

Figure 1. Block diagram of the system.

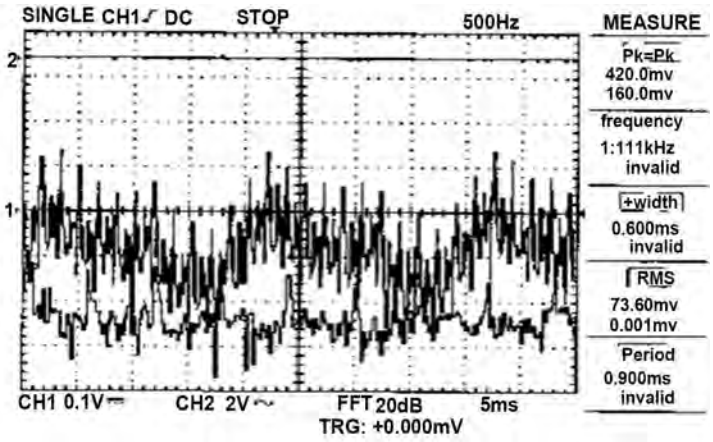

Figure 2. The signal recorded by digital oscilloscope for first (BCC) tissue.

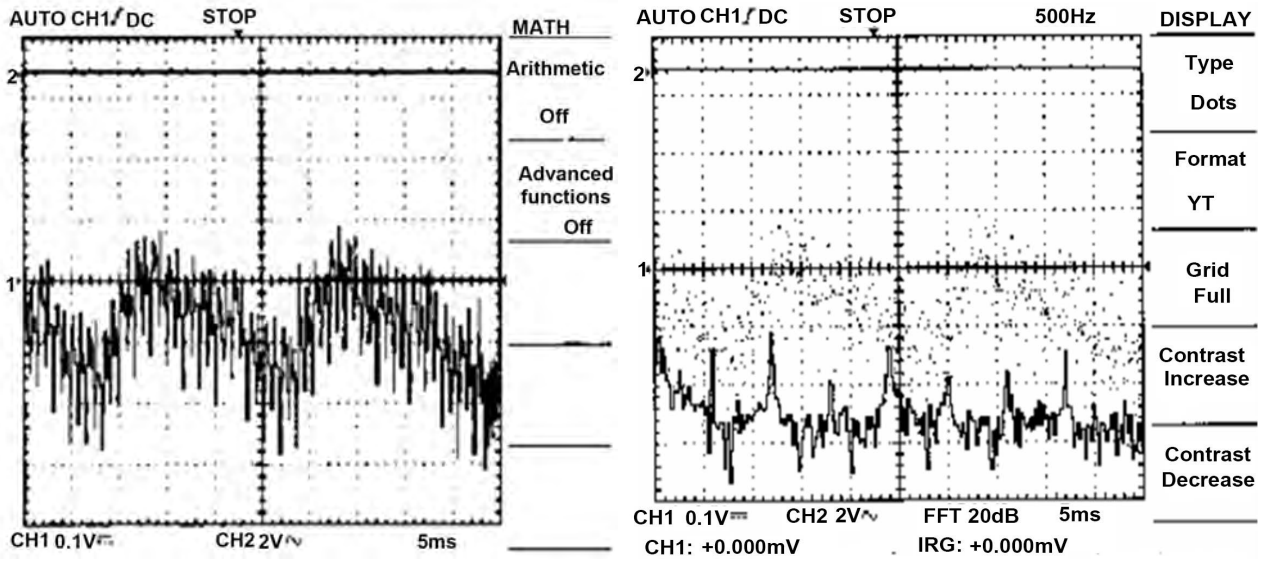

(a) (b)

Figure 3. The signal recorded by digital oscilloscope for second (BCC) tissue. (a) In normal ordinate; (b) In Fourier frequency.

Figure 4 shows the tissue signal, (a) in normal ordinate before FT, while (b) after FT. Information's displayed on digital oscilloscope for third (BCC) sample are frequency 1.25 kHz, peak 396 mv, width 0.6 ms and period 0.8 ms.

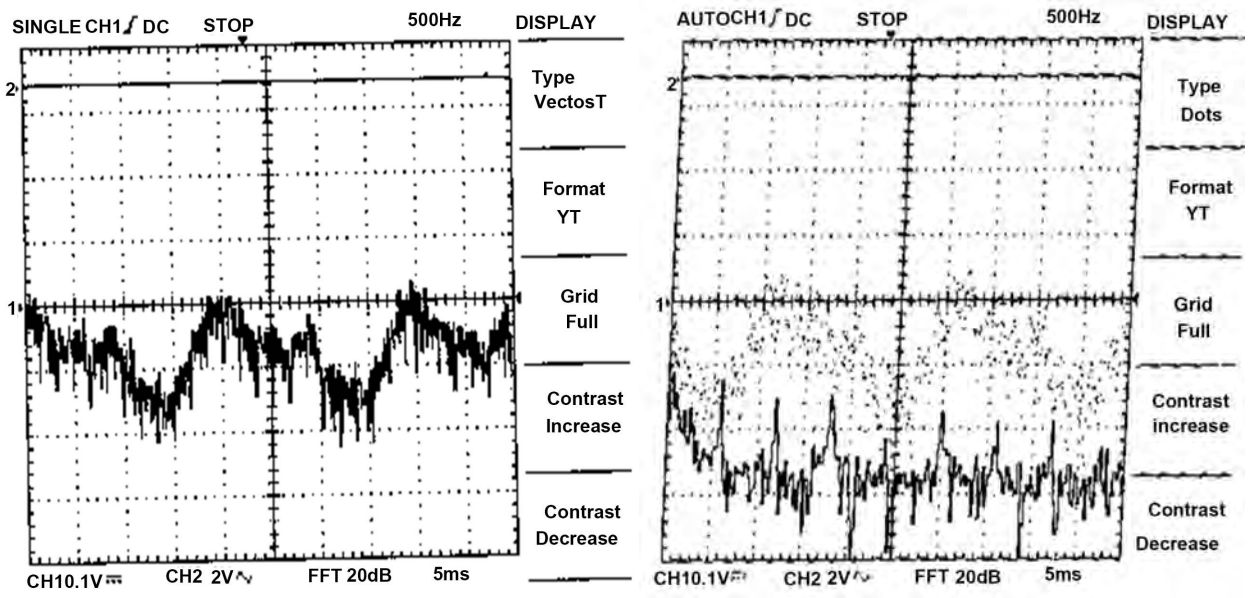

(a) (b)

Figure 4. The signal recorded by digital oscilloscope for third (BCC) tissue. (a) In normal ordinate; (b) In Fourier frequency.

Figure 5 shows the tissue signal, (a) in normal ordinate before FT, while (b) after FT. Information's displayed on digital oscilloscope for fourth (BCC) sample are frequency 833.3 Hz, peak 268 mv, width 0.6 ms, period 1.2 ms.

From the signals recorded by digital oscilloscope for studied samples we notice:

Third tissue has the highest peak, while the first one has the lowest one. Also third tissue has a short period (0.8 ms), which lead to high frequency (Table 1).

From the above results one can see that the optical coherence tomography system (OCTS) can be used to determine the depth resolution and the transverse resolution [26], in longitudinal direction with good performance for different tissues.

According to the above table, longitudinal resolution is higher than transverse resolution for all samples.

Third tissue has the biggest resolution (longitudinal resolution 0.5624 μm, transverse resolution 0.422 μm) and the minimum for fourth tissue.

From the variation of the intensity with distance, in order to obtain a spectral tomography of the objects [27] [28].

Optical properties can be determined by fitting linear or logarithm function. Figures 6-9 show this variation, while Table 2 illustrates the optical properties for the samples.

There are considerable difference in the optical properties of various types of tissue and even more significant difference in the same tissue at different wavelength [10]. Figures illustrated the lowest backscattered signal for the fourth.

Table 2 shows the highest absorption coefficient for second and fourth tumors, which lead to low penetration depth.

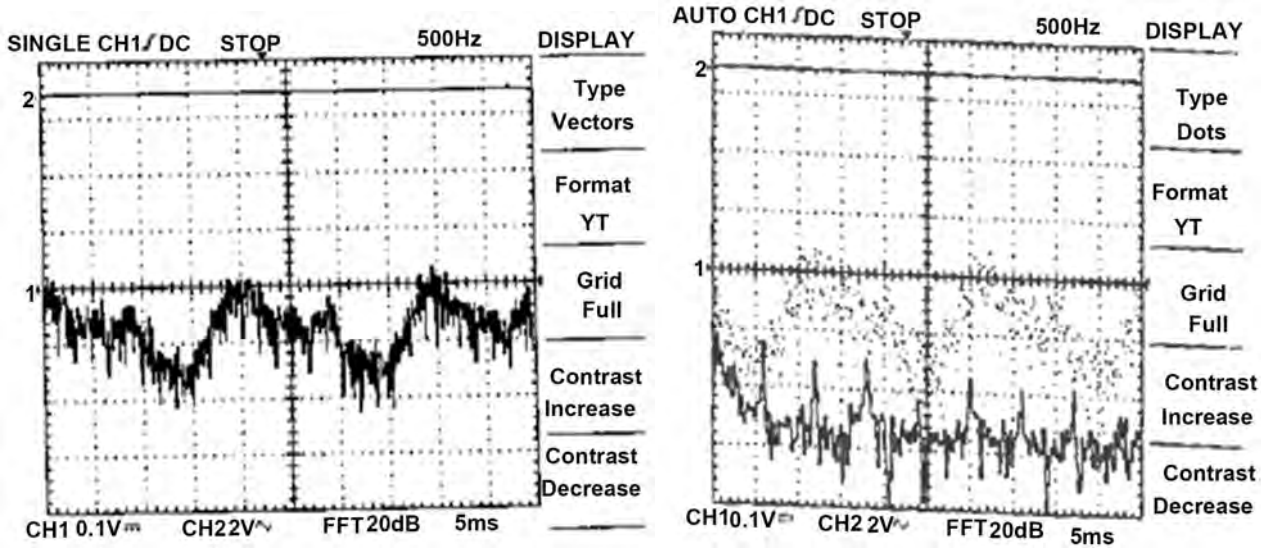

(a) (b)

Figure 5. The signal recorded by digital oscilloscope for fourth (BCC) tissue. (a) In normal ordinate; (b) In Fourier frequency.

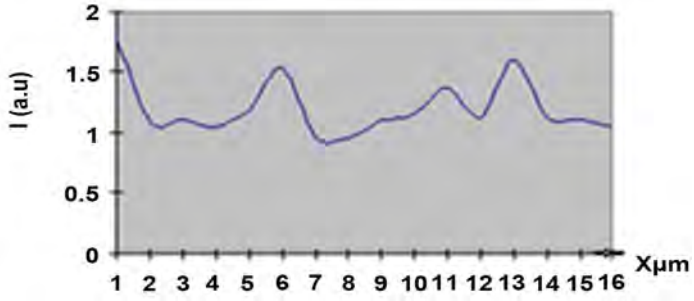

Figure 6. Intensity of the backscattered light as a function of the depth for the First basal cancer.

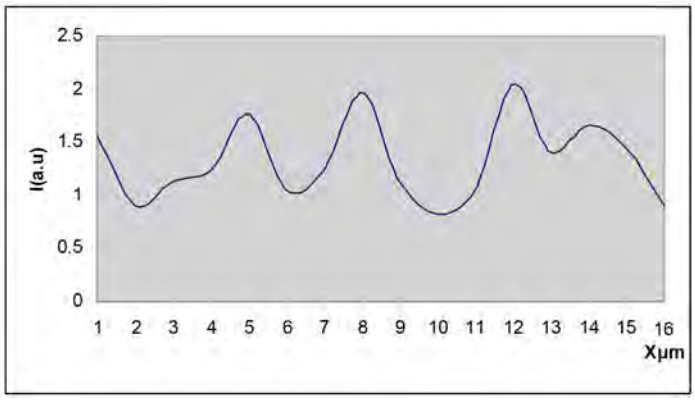

Figure 7. Intensity of the backscattered light as a function of the depth for the second basal cancer.

4. Conclusions

1) OCT can be considered as new modality in cancer diagnosing because of its safe considerations and its ability to be applied *in vivo*.

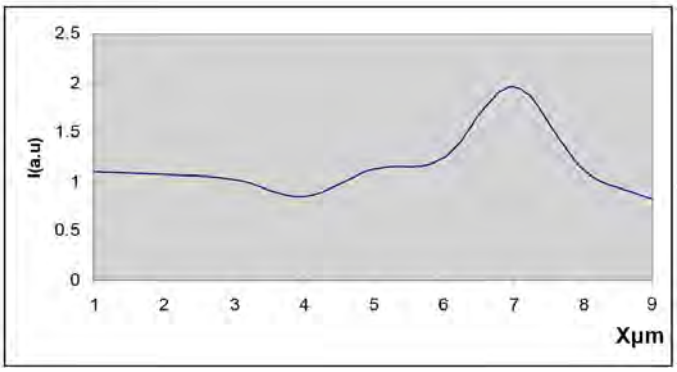

Figure 8. Intensity of the backscattered light as a function of the depth for the Third basal cancer.

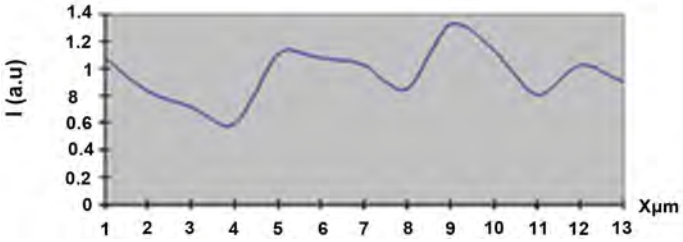

Figure 9. Intensity of the backscattered light as a function of the depth for the Forth basal cancer.

Table 1. List the samples results calculated from **Figures 2-5**.

|Samples	R R(μm) depth resolution	ΔLB(μm) spatial resolution
Basal cancer	0.37967	0.2832
Basal cancer	0.4398	0.3329
Basal cancer	0.5624	0.422
Basal cancer	0.368	0.259

Table 2. Samples optical properties.

(a)

Object type	Penetration depth (mm)	Absorption coefficient (mm^{-1})	Attenuation coefficient (mm^{-1})	Scattering coefficient (mm^{-1})
Tissue (1)	0.062	12.375	16.129	3.754
Tissue (2)	0.031	30.800	32.258	1.458
Tissue (3)	0.0605	14.000	16.529	2.529
Tissue (4)	0.030	30.130	33.333	3.333

(b)

Object type	Reduced scattering coefficient (mm^{-1})	Reduced attenuation coefficient (mm^{-1})	Reduced penetration depth (mm)
Tissue 1	7.504	19.883	0.050294
Tissue 2	2.916	33.716	0.02966
Tissue 3	5.058	19.058	0.05247
Tissue 4	6.667	36.667	0.02727

2) (OCTS) technique can be used to get information of internal structure of the tissue, the contents of the tissue cells and its concentration.

3) The optical properties of different tissues can be determined using OCT.

5. Recommendations

Other types of optical tomography techniques can be used to estimate the most efficient one in determination of the optical properties of tissues.

Automatic scanning system can be used to perform good scanning for samples, so that the thickness information of the tissues can be gained with good accuracy.

Acknowledgements

Deep thanks to Cancer Center and National Institute of Laser Enhanced Science, Cairo University, Egypt.

Conflicts of Interest

The authors declare no conflicts of interest regarding the publication of this paper.

References

[1] Alejandro, G.U., Jun, Z., Madeleine, D., Jeong H.C., Victor, G.P. and Lihong, V.W. (2012) *In Vivo* Diagnosis of Melanoma and Nonmelanoma Skin Cancer Using Oblique Incidence Diffuse Reflectance Spectrometry. American Association for Cancer Research.

[2] Elena, S., Brian, J., John, N. and Anna, N.Y. (2006) Optical Properties of Normal and Cancerous Human Skin in the Visible and Near-Infrared Spectral Range. *Journal of Biomedical Optics*, **11**, 064026. https://doi.org/10.1117/1.2398928

[3] Flohil, S.C., de Vries, E., Neumann, H.A., Coebergh, J.W. and Nijsten, T. (2011) Incidence Prevalence and Future Trends of Primary Basal Cell Carcinoma in the Netherlands. *Acta Dermato Venereologica*, **91**, 24-30. https://doi.org/10.2340/00015555-1009

[4] Roewert, H.J., Lang, A.B., Stockfleth, E. and Kerl, H. (2007) Epidemiology and Aetiology of Basal Cell Carcinoma. *British Journal of Dermatology*, **157**, 47-51. https://doi.org/10.1111/j.1365-2133.2007.08273.x

[5] Takata, M. and Saida, T. (2005) Early Cancers of the Skin Clinical Histopathological and Molecular Characteristics. *International Journal of Clinical Oncology*, **10**, 391-397. https://link.springer.com/article/10.1007/s10147-005-0532-7 https://doi.org/10.1007/s10147-005-0532-7

[6] Marc, B., Mariano, S., Makiko, M., Alice, M., Gregor, J. and Veronique, D.M. (2016) *In Vivo* Assessment of Optical Properties of Basal Cell Carcinoma and Differentiation of BCC Subtypes by High-Definition Optical Coherence Tomography. *Biomedical Optics Express*, **7**, 2269-2284. https://www.osapublishing.org/boe/abstract.cfm https://doi.org/10.1364/BOE.7.002269

[7] Carsin, A.E., Sharp, L. and Comber, H. (2011) Geographical Urban/Rural and Socioeconomic Variations in Nonmelanoma Skin Cancer Incidence a Population-Based

Study in Ireland. *British Journal of Dermatology*, **164**, 822-829.
https://www.ncbi.nlm.nih.gov/pubmed/21291423
https://doi.org/10.1111/j.1365-2133.2011.10238.x

[8] Sellheyer, K. (2011) Basal Cell Carcinoma Cell of Origin, Cancer Stem Cell Hypothesis and Stem Cell Markers. *British Journal of Dermatology*, **164**, 696-711.
https://www.ncbi.nlm.nih.gov/pubmed/21128907
https://doi.org/10.1111/j.1365-2133.2010.10158.x

[9] Trakatelli, M., Morton, C., Nagore, E., Ulrich, C., Delmarmol, V., Peris, K. and Basset, S.N. (2014) BCC Subcommittee of the Guidelines Committee of the European Dermatology Forum, Update of the European Guidelines for Basal Cell Carcinoma Management. *European Journal of Dermatology*, **24**, 312-329.
https://doi.org/10.1684/ejd.2014.2271

[10] Cameron, H.G., Steven, F.B. and Ashely, J.W. (1999) Laser Tissue Interaction, U.S.A.

[11] Lihong, V.W. and Qimin, S. (1999) Sonoluminescence Tomography of Turbid Media. *SPIE*, Vol. 359, San Jose, California. https://doi.org/10.1684/ejd.2014.2271

[12] Mehreen, A. and Jay, S.D. (2013) Optical Coherence Tomography: Current and Future Applications. US National Library of Medicine National Institutes of Health. *Current Opinion in Ophthalmology*, **24**, 213-221.
https://doi.org/10.1097/ICU.0b013e32835f8bf8

[13] David, T. (2018) What Is Optical Coherence Tomography? American Academy of Ophthalmology.
https://www.aao.org/eye-health/treatments/what-is-optical-coherence-tomography

[14] Thomsen, J.B., Sander, B., Mogensen, M., Thrane, L., Jørgensen, T.M., Jemec, G.B.E. and Andersen, P.E. (2009) Optical Coherence Tomography Technique and Applications. Springer-Verlag Berlin Heidelberg.
https://doi.org/10.1007/978-3-540-68993-5_5

[15] Danielson, B.L. and Whittenberg, C.D. (1987) Guide Wave Reflectometry with Micrometer Resolution. *Applied Optics*, **26**, 2836-2842.
https://www.osapublishing.org/abstract.cfm?uri=ao-26-14-2836
https://doi.org/10.1364/AO.26.002836

[16] Falco, M.D., Lepore, M. and Indovina, P.L. (2000) Difference in Optical Properties of Normal and Tumoral Tissues: A Comparison to Accuracy Limits in Laser Techniques for Optical Imaging. *Proceedings of SPIE*, **4160**.

[17] Laubscher, M., Ducros, M., Karamata, B., Lasser, T. and Salathé, R. (2002) Video-Rate Three-Dimensional Optical Coherence Tomography. *Optics Express*, **10**, 429-435. https://www.osapublishing.org/viewmedia.cfm?uri=oe-10-9-429

[18] Ko, T.H., Witkin, A.J., Fujimoto, J.G., Chan, A., Rogers, A.H., Baumal, C.R., Schuman, J.S., Drexler, W., Reichel, E. and Duker, J.S. (2002) Ultrahigh-Resolution Optical Coherence Tomography of Surgically Closed Macular Holes. *Archives of Ophthalmology*, **124**, 827-836. https://doi.org/10.1001/archopht.124.6.827
https://www.ncbi.nlm.nih.gov/pmc/articles/PMC1937370/

[19] Hitzenberger, C.K., Kuihavy, M., Lexer, F., Baumgartner, A. and Fercher, A.F. (1998) *In Vivo* Intraocular Ranging by Wavelength Tuning Interferometery. *Proceedings of SPIE*, **3251**, 47-51.

[20] Choi, E., Kim, Y.-J., Kim, M.J., Lee, C. and Lee, B.H. (2003) OCT Resolution Enhancement Using Long Period Fiber Grating and Erbium-Doped Fiber. *Proceedings of SPIE*, **4956**.

[21] Riza, N.A. and Yaqoob, Z. (2000) High-Speed No-Moving-Parts Optical Coherence

Tomography System. *Proceedings of SPIE*, **4160**.

[22] Takada, K., Yokohama, I., Chida, K. and Noda, J. (1987) New Measurement System for Fault Location in Optical Waveguide Devices Based on an Interferometric Technique. *Applied Optics*, **26**, 1603-1606. https://www.ncbi.nlm.nih.gov/pubmed/20454375 https://doi.org/10.1364/AO.26.001603

[23] Fercher, A.F. (1996) Optical Coherence Tomography. *Journal of Biomedical Optics*, **1**, 157-173. https://doi.org/10.1117/12.231361

[24] Dean, P., Dickinson, M.R. and West, D.P. (2003) Optical Coherence Tomography Using a Photorefractive Polymer Composite. *Proceedings of SPIE*, **4956**.

[25] Huang, D., Swanson, E.A., Lin, C.P., Schuman, J.S., Stinson, W.G., Chang, W., Heee, M.R., Flotte, T., Gregory, K., Pulifito, C.A. and Fujimoto, J.G. (1991) Optical Coherence Tomography. *Science*, **254**, 1178-1181. https://doi.org/10.1126/science.1957169

[26] Fujimoto, J.G. (2001) Optical Coherence Tomography. *Applied Physics*, **2**, 1099-1111.

[27] Leitgeba, R., Wojtkowskib, M., Hizenbergera, C.K., Ferchera, A.F., Stickera, M. and Kowalezykb, A. (2000) Depth Resolved Spectroscopy by Frequency Domain Optical Coherence Tomography. *Proceedings of SPIE*, **4160**, 57-61. https://doi.org/10.1117/12.407608

[28] Hitzenberger, C.K. (1991) Optical Measurement of the Axial Eye Length by Laser Doppler Interferometery. *Investigative Ophthalmology & Visual Science*, **32**, 616-624.

Scientific Research Publishing

Open Journal of Biophysics, 2019, 9, 98-109
http://www.scirp.org/journal/ojbiphy
ISSN Online: 2164-5396
ISSN Print: 2164-5388

Bioelectromagnetic Paradigm of Cancer Treatment—Modulated Electro-Hyperthermia (mEHT)

Oliver Szasz

Department of Biotechnics, St. Istvan University, Budaörs, Hungary
Email: biotech@gek.szie.hu

How to cite this paper: Szasz, O. (2019) Bioelectromagnetic Paradigm of Cancer Treatment—Modulated Electro-Hyperthermia (mEHT). *Open Journal of Biophysics*, **9**, 98-109.
https://doi.org/10.4236/ojbiphy.2019.92008

Received: January 28, 2019
Accepted: February 24, 2019
Published: February 27, 2019

Abstract

One of the most frequently applied bioelectromagnetic effects is the deep heating of the living species with EMF energy. Despite its long history, hyperthermia is a rarely applied oncotherapy. The reason is its controversial results and complicated control. One of the solutions is concentrating the electromagnetic energy nanoscopically on the parts of the malignant cells instead of heating up the complete tumor-mass. This approach is a kind of non-uniform energy absorption, providing energy liberation only in the selected regions. The energy-absorption of the malignant cells targets the membranes and creates a situation far from thermal equilibrium. The selection of the malignant cells is based on their decided differences from their healthy counterparts. The distinguishing parameters are the electromagnetic properties of the components of the malignant tissue which are the physiologic differences between the malignant cells and their healthy counterparts. The targets realize nano-range heating, using natural nanoclusters on the cell-membrane without artificially implementing them. This energy absorption generates consequent reactions, like programmed cell-death (apoptosis) continued by immunogenic cell-death involving extended immune reactions. The applied radiofrequency current is amplitude modulated by time-fractal modulation pattern. The accurately matched impedance realizes the self-selective mechanisms which are promoted by stochastic resonances. This complex method is a new kind of hyperthermia, named mEHT. Our objective is to analyze the problems of the selective, non-equilibrium energy absorption, and present a solution by the electromagnetic mechanisms for an effective and controllable hyperthermia in oncology.

Keywords

Electromagnetic Effects, RF-Current, Warburg-Effect, Szent-Gyorgyi-Effect,

Fractal-Physiology, Oncology, Hyperthermia, Nanoscale Heating, Modulated Electro-Hyperthermia, Nanothermia, mEHT, Apoptosis, Immunogenic Cell-Death

1. Introduction-Hyperthermia Challenges

Modern hyperthermia treatments in oncology use electromagnetic effects overheating the living object completely (whole body) or partly (regionally or locally). Oncological hyperthermia is intended to be an ideal combination therapy; it provides synergies with most of the conventional treatment modalities, boosts their efficacy and helps to desensitize the previously non-effective treatments.

The history of hyperthermia in oncology has been hectic and controversial [1]. In consequence, the general professional skepticism blocked its application for a long time. Hyperthermia is a constrain energy-delivery, forcing the homeostatic equilibrium to change. From this point the control of the processes became complicated. The adequate dose and protocol of the method and the reproducibility of the results are a complex task; its thermal status is far from equilibrium.

There are multiple physiologic feedbacks trying to re-establish the lost homeostasis. The main correction factors in the thermal control are the blood-flow and the surface regulation processes, like the sweating, orientation control of the hair in the skin, etc. The local heating immediately activates the physiological controls, first of all, the blood-flow, creating intensive heat-exchange conditions to construct a local out-of-equilibrium situation.

The locally or systemically increased blood-flow tries to compensate the growing temperature and cools down the target volume. The blood-flow drastically modifies the specific absorption rate (SAR), irrespective of how accurately it was focused on the tumor-mass. In consequence, the SAR and the temperature mapping of the targeted volume could be significantly different. Therefore, competition starts between the cell-killing potential of the heat and the cancer-supporting potential of the gained blood-supply by higher temperature of the targeted volume.

The focus of the RF-energy is not an easy task, but not impossible. However, the focus of the energy does not mean the focus of the temperature. The temperature is naturally spread by the convective and conductive heat-flow, derived from the temperature gradient and controlled by the physiologic constrains. Temperature-spread is a natural process, its termination is impossible. The time limit is only the heated volume. This is how the ablation techniques work. Also, the isotherms of the heating can be defined only with the help of the time-factor.

Following the temperature distribution is a safety issue, it is important to block the local burn of the healthy tissue, while allowing the temperature for necrosis in the tumor. The temperature control shows the temperature spreading

well, as well as the formation of the unwanted and uncontrolled hot-spots [2], [3].

Together with the problems of the temperature measurement in depth of the body to control the target, the technical solutions of the energy delivery are also challenging, due to the fact that the deep-heating needs complicated bioelectromagnetic considerations. The energy has to be delivered in depth without overheating the healthy layers between and has to be focused in depth on the heterogeneous and non-regular form of the tumor. The penetration depth of the biological material has frequency dispersion, quickly shortened by the growing frequency, and so contradicting with the demand of high frequency for precise beaming. The bolus-transmitters have to be constructed and non-absorbing but well transferring of the applied electromagnetic effects and the temperature of the body surface has to be limited under the blistering threshold.

To provide enough energy in depth, it needs power of >20 W/kg [4], which is far over the surface tolerance. Usually intensive cooling of the surface is applied to avoid the blisters on the skin. This method has also various physiological feedbacks. When the cooling is too large, the feedback isolates the skin from the deeper cooling, reducing the blood-flow in the subcutane layer under the cooled area. The extra impedance requests higher voltage to provide the same power in the depth as before, increasing the skin jump of the electric field vector perpendicular to the surface. The increased potential will increase the risk of burn.

Due to the challenges, many prospective clinical trials of conventional hyperthermia are questioned [5]. A recognized specialist of hyperthermia formulated a long time ago [6]: "The mistakes made by the hyperthermia community may serve as lessons, not to be repeated by investigators in other novel fields of cancer treatment."

The modulated electro-hyperthermia (mEHT, trademark: oncothermia) offers a new paradigm with nanoscopic heating having adequate answer to the present complex challenges.

2. Method-Selection Parameters in Nanoscopic Range

During conventional hyperthermia applications the macroscopic heating concentrates on the equal (homogeneous) temperature of the entire targeted volume or at least it constructs isothermal (isodose) patterns. The above described physiological feedbacks and the very inhomogeneous malignant target make this aim impossible. mEHT as new paradigm of hyperthermia technology declares the non-equal heating, it does not try to reach any macroscopic "isotherm" actionsas usual goal in ionizing radiation. The isotherms are consequences of the "bad reflex" of the equilibrium effects. Due to its heterogeneity, heating in biosystems are anyway far from equilibrium, when the physiological feedback as well as the normal thermodynamical rules are contracting of the macroscopic equilibrium. The method, mEHTdoes not heat the complete tissue in the targeted volume equally [7]. It concentrates the liberation of the absorbed energy

on the cellular membranes and on the extracellular electrolytes of malignant cells [8]. The microscopically inhomogeneous heating is far from the thermal equilibrium [9]. MEHT applies cellular approach selectively, heating up the malignant cells individually liberating the incident energy in nanoscopic range at the cell-membrane [10]. The energy-absorbers are the membrane rafts, which are clusters of transmembrane proteins, populating the membrane of malignant cells more densely than of the cells of the healthy counterparts. This method does not need any artificially implemented nanomaterials into the target, it uses natural nanoscopic clusters of membrane rafts [11]. Experimental verification of this method shows the significant inducement of apoptosis by this method on lower average temperatures than the isothermal heating does, [12].

The heating energy is not liberated in a sudden single step but is regulated in multiple small energy-absorption processes. This makes it possible to control the energy-liberation and to avoid the overheating the healthy parts. The accurate selection of malignant cells is a key step in the proper mEHT. There are robust electromagnetic differences between the malignant and healthy cells *in vivo*. The biological processes and structures of the healthy cells are distinguishably different from the malignant ones. These differences make it possible to accurately select the cancer-cells by their electromagnetic behaviors and actively destroy them without damages on their healthy neighborhood.

The main physiological differences between malignant cells and their healthy counterparts are:

1) Differences in the metabolic rate of the malignant and healthy cells (Warburg effect, [13]), which create higher conductivity of tumor than its neighborhood. The increase of the current density in the tumor could be visualized by the measurements of real processes by radiofrequency current density image (RF-CDI), [14] [15] [16] [17]. The Electric Impedance Tomography (EIT) measures and images the tumor based on the impedance differences [18]. This effect could be applied in prophylactics like mammography [19]. Further increase of the conduction selectivity is the positive feedback by growing temperature, [20]. The measured gain of selectivity is active [21], which means 14% increase by heating of $36^{\circ}C \rightarrow 43^{\circ}C$.

2) Differences in the dielectric constant of the extracellular electrolyte and membrane-bound water of the malignant and healthy cells (Szent-Gyorgyi effect, [22]); which allows the selection of malignant cells by their autonomy caused higher dielectric permittivity. The cell-cell adhesion is decreased by the increasing permittivity, [23], which harmonizes with the autonomic malignant cells (disorder in extracellular matrix [24]) and their decreased membrane potential, [25]. The order-disorder phase-transition indicates two different states of the cells: their autonomy status (called alpha-state) and their connected collective status (beta-state), [26].

3) The above two are combined with delta/beta dispersion (Schwan effect) [27]); to select the transmembrane protein clusters (rafts) of malignant cells. There are

various forms of frequency dependent energy-absorption mechanisms exist, [28], creating variation of the dielectric properties, [29]. The β-dispersion [30] (known as interfacial polarization effect) is between 0.1 - 100 MHz, it is characteristically determined by the membrane capacities of the cell and the intracellular organelles, bound-water to membrane etc. Responses in this interval are well-connected to the cell-membrane changes. The bound water to the membrane has the upper frequency part of the β-dispersion, denoted by δ, [31], and so this part is well-selective for the various cell-membrane states. Selective treatments have to be chosen in range of β-dispersion, [32]. Especially, the difference between the malignant and healthy tissue is that all the electrolyte and membrane properties differ, [33] [34]. The proper selection uses the dipole relaxation of beta-dispersion connected to the membrane bounded water, [35].

4) Structural differences (pathological pattern recognizing) between the malignant and healthy tissues (fractal physiology effect, [36]). The morphology is an important factor of the cellular organization, [37], and varies by kind of tissues. Cellular structures have coordination constrains preferring special coordination arrangements [38], and form self-organized collectivity [39] [40]. The tendency of proliferation is low in the population having small number of cells [41]. A critical cell density is necessary when starting significant cell division, similarly to the observed self-synchronization of chemical oscillators [42]. Dominantly, a favorable topological position (cyclic symmetry of the coordination number) chooses the actual division [43]; justified experimentally too, [44]. Healthy cells work collectively, their energy-consumption, as well as their life-cycles and the availability of resources are controlled in collective way by the various forms of the self-organizing, [45]. The organization process is governed by special "social" signals [46] commonly regulating and controlling the system. The self-organizing in topology is connected to a fractal-structure, which also appears in the dynamic self-similar stochastic behavior of the system, [47].

The special selection effects described above are accurately applied in mEHT, briefly summarized in **Figure 1**. However, the dose of energy is crucial for all the selection steps. Applying too much energy realizes the classical hyperthermia, it heats up all components of the target, the treatment loses its selection ability. The popular wisdom is valid: the difference between the medicine and poison is only the applied dose.

3. Results-Technical Realization of Nano-Heating

MEHT uses the above selection factors targeting the malignant cells with high efficacy, heating it to high temperature very locally (nanoscopic range) and stimulating the immune reactions against the malignant metastases. While the conventional hyperthermia focuses on and targets a macro region, the nano-heating of mEHT process, is similar to the ionizing radiation concept, which also acts nanoscopically on the DNA of the cells. Radiotherapy destroys the DNA strands, nanotherapy of mEHT destroys the cell-membrane of the malignant cell

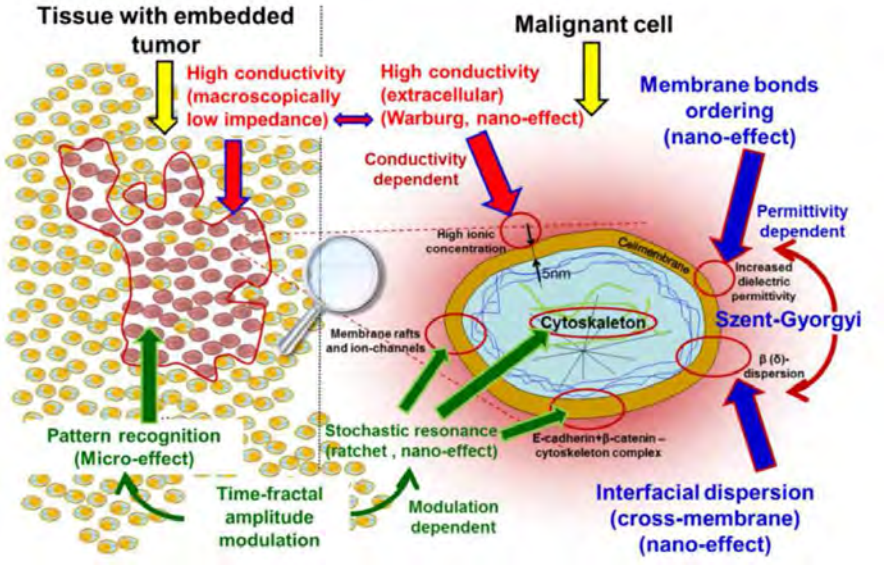

Figure 1. Main selection factors of modulated electrothermia (nanothermia, mEHT) method (to be clear, only those details are shown, which have role in the processes) {Adapted from [48]}.

or at least induces apoptotic cell death from there, due to the energy-absorption on the clusters of transmembrane proteins, as nanounits.

The electric effects are shown on a schematic impedance figure (**Figure 2**). The various actions are not independent, effects are overlapping and synergetic.

Heating of the ECM more intensively than the cytoplasm provides a spherical thermal gradient and consequently creates heat-flow through the membrane of all the selected individual cells. This centrally symmetric effect avoids the thermal limit of the external field application [49].

This nanoheating is far from thermal equilibrium. According to the Onsager's reciprocity relations [50], the induced heat-flow is coupled to charge current too, as well as the kinetics of the processes is also coupled, [51]. This current is ~150 pA/μm^2, [52]. This ionic current creates a zero-mode electric current, which in turn induces a zero-mode electric field in the cell membrane. Therefore, even small fields with zero-th mode components could elicit biological effects.

The temperature gradient through the cellular membrane pumps the non-equilibrium thermal processes. The gradient is quite large (~0.01˚C /nm [≈ 107˚C/m]), [46], creating a considerable heat-flow (~1.5 pW/μm^2). One of the actions is the change of the intracellular pressure (1320 kPa; [46]); by the electro-osmotic conditions. Due to the rigid cell membrane of the cancerous cells [53], the pressure could be fatal for the cell which has maximal tolerable lateral tensile stress of σmax ≈ (2 − 10)105 Pa [54]. The high pressure (when it is not enough to explode the cell) increases the membrane permeability, allowing the internal HSP chaperones to be expressed on the outer membrane to ignite immune reactions. This process is promoted by the temperature effect on the membrane permeability.

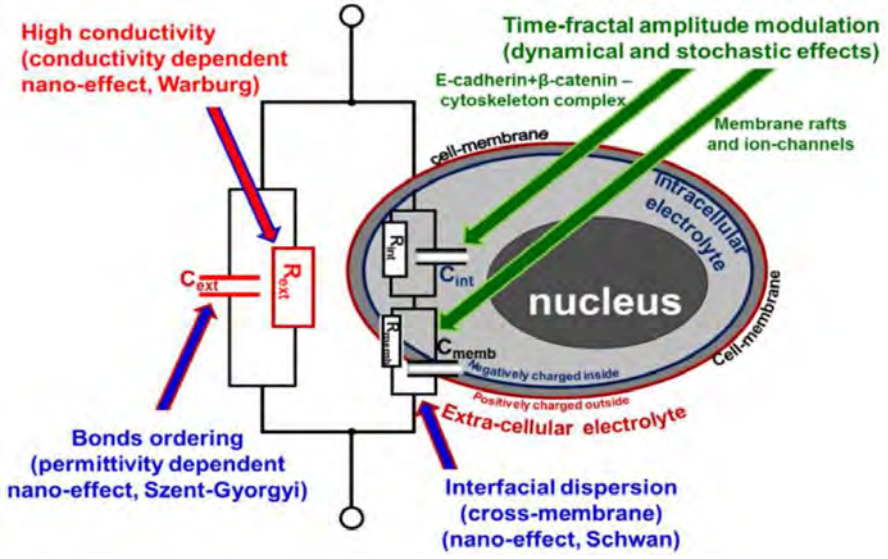

Figure 2. Action of the various selection factors in nanothermia shown in the impedance schematics of a malignant cell {Adapted from [48]}.

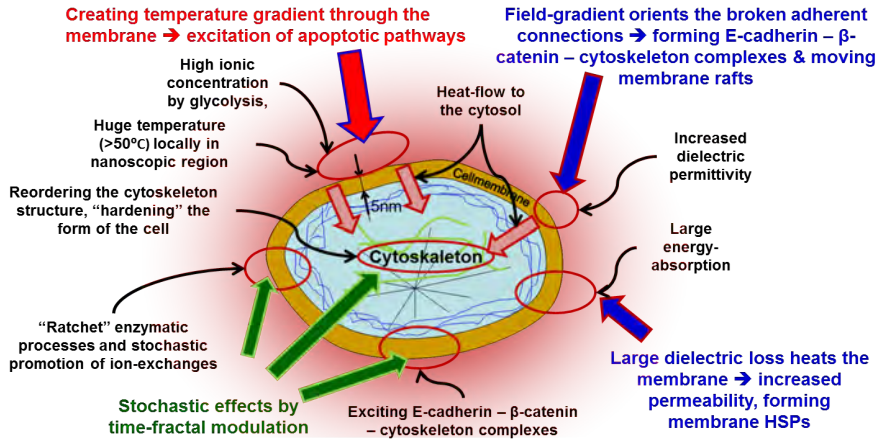

Figure 3. Summary of mEHT selection effects on malignant cell {Adapted from [48]}.

The RF-current anyway has special effects characteristically acting on the membrane of the cells. Its ohmic component directly affects the membrane, while the displacement current (imaginary component) deflects it, causing various mechanical effects on the outer membrane. The effect of the ohmic component is proportional with the square of the RF-current (Joule heat) while the capacitive component simply depends on the current itself. The summary of the effects is shown on **Figure 3**.

The synergy of electric field with the thermal effects selectively acts on the malignant cells and could be well followed from laboratory to the patient's bed, [55]. The certain differences between the mEHT and other hyperthermia with the same temperature are clearly shown by *in vitro* [56] and *in vivo* [57] measurements. The immune-simulative effect of the method is also proven [58]. The method has wide and successful clinical applications in various cancer types, like gliomas [59], colorectal cancers, [60] [61]; lung cancers [62] [63], in carcinoma

of uterine cervix [64], malignant ascites [65], sarcomas [66] [67], pancreas carcinoma [68] [69]; prostate cancer [70] [71].

4. Conclusion

Bioelectric explanation of heterogeneric heating of mEHT method is discussed. The method uses nanoheating technology to select and effectively heat the rafts of transmembrane proteins on the membrane of the malignant cells. The bioelectromagnetic selection focuses the electromagnetic absorption on the cell-membranes. The nano-range energy-liberation could be precisely controlled without considerable wasted energy and without having disadvantages because of the heating of the tumor-environment on average. MEHT results and its general benefits open a new kind of local heating to destroy the primary and metastatic tumor lesions.

Acknowledgements

This work was supported by the Hungarian Competitiveness and Excellence Programme grant (NVKP_16-1-2016-0042).

Conflicts of Interest

The author declares no conflicts of interest regarding the publication of this paper.

References

[1] Roussakow, S. (2013) The History of Hyperthermia Rise and Decline. *Conference Papers in Medicine*, **2013**, Article ID 428027.

[2] Gellermann, J., Wlodarczyk, W., Hildebrandt, B., Ganter, H., Nicolau, A., Rau, B., Tilly, W., Fähling, H., Nadobny, J., Felix, R. and Wust, P. (2005) Noninvasive Magnetic Resonance Thermography of Recurrent Rectal Carcinoma in a 1.5 Tesla Hybrid System. *Cancer Research*, **65**, 5872-5880. https://doi.org/10.1158/0008-5472.CAN-04-3952

[3] Wust, P., Hildebrandt, B., Sreenivasa, G., Rau, B., Gellermann, J., Riess, H., Felix, R. and Schlag, P.M. (2002) Hyperthermia in Combined Treatment of Cancer. *Lancet Oncology*, **3**, 487-497. https://doi.org/10.1016/S1470-2045(02)00818-5

[4] Wust, P. (2005) Thermoregulation in Humans, Experiences from Thermotherapy. *Conference in Stuttgart*, Stuttgart, Germany, 21 November 2005.

[5] Roussakow, S. (2013) Critical Analysis of Electromagnetic Hyperthermia Randomized Trials: Dubious Effect and Multiple Biases. *Conference Papers in Medicine*, 2013, Article ID 412186.

[6] Storm, F.K. (1993) What Happened to Hyperthermia and What Is Its Current Status in Cancer Treatment? *Journal of Surgical Oncology*, **53**, 141-143. https://doi.org/10.1002/jso.2930530302

[7] Szasz, A. (2013) Challenges and Solutions in Oncological Hyperthermia. *Thermal Medicine*, **29**, 1-23. https://doi.org/10.3191/thermalmed.29.1

[8] Szasz, O. and Szasz, A. (2013) Essentials of Oncothermia. *Conference Papers in Medicine*, **2013**, Article No. 159570.

[9] Szasz, A., Vincze, Gy., Szasz O, and Szasz, N. (2003) An Energy Analysis of Extracellular Hyperthermia. *Electromagnetic Biology and Medicine*, **22**, 103-115.

https://doi.org/10.1081/JBC-120024620

[10] Szasz, O. and Szasz, A. (2014) Oncothermia-Nano-Heating Paradigm. *Journal of Cancer Science & Therapy*, **6**, 117-121. https://doi.org/10.4172/1948-5956.1000259

[11] Vincze, Gy., Szigeti, Gy., Andocs, G. and Szasz, A. (2015) Nanoheating without Artificial Nanoparticles. *Biology and Medicine*, **7**, 249.

[12] Andocs, G., Rehman, M.U., Zhao, Q.L., Papp, E., Kondo, T. and Szasz, A. (2015) Nanoheating without Artificial Nanoparticles Part II. Experimental Support of the Nanoheating Concept of the Modulated Electro-Hyperthermia Method, Using U937 Cell Suspension Model. *Biology and Medicine*, **7**, 247. https://doi.org/10.4172/0974-8369.1000247

[13] Warburg, O. (1966) Oxygen, the Creator of Differentiation. Academic Press, New York.

[14] Mikac, U., Demsar, F., Beravs, K. and Sersa, I. (2001) Magnetic Resonance Imaging of Alternating Electric Currents. *Magnetic Resonance Imaging*, **19**, 845-856. https://doi.org/10.1016/S0730-725X(01)00393-9

[15] Joy, M., Scott, G. and Henkelman, M. (1989) *In Vivo* Detection of Applied Electric Currents by Magnetic Resonance Imaging. *Magnetic Resonance Imaging*, **7**, 49-54. https://doi.org/10.1016/0730-725X(89)90328-7

[16] Seersa, I., Beravs, K., Dodd, N.J., Zhao, S., Miklavcic, D. and Demsar, F. (1997) Electric Current Density Imaging of Mice Tumors. *Magnetic Resonance in Medicine*, **37**, 404-409. https://doi.org/10.1002/mrm.1910370318

[17] Scott, G.C., Joy, M.L.G., Armstrong, R.L. and Henkelman, R.M. (1995) Electromagnetic Considerations for RF Current Density Imaging [MRI Technique]. *IEEE Transactions on Medical Imaging*, **14**, 515-524. https://doi.org/10.1109/42.414617

[18] Babaeizadeh, S. (2007) 3-D Electrical Impedance Tomography for Piecewise Constant Domains with Known Internal Boundaries. *IEEE Transactions on Biomedical Engineering*, **54**, 2-10. https://doi.org/10.1109/TBME.2006.886839

[19] TransCan, T.S. and Transcan, Medical Ltd. (2000)

[20] McRae, DA., Esrick, M.A. and Mueller, S.C. (1997) Non-Invasive, *In-Vivo* Electrical Impedance of EMT-6 Tumours during Hyperthermia: Correlation with Morphology and Tumour-Growth-Delay. *International Journal of Hyperthermia*, **13**, 1-20. https://doi.org/10.3109/02656739709056426

[21] Esrick, M.A. and McRae, D.A. (1994) The Effect of Hyperthermia-Induced Tissue Conductivity Changes on Electrical Impedance Temperature Mapping. *Physics in Medicine and Biology*, **39**, 133-144. https://doi.org/10.1088/0031-9155/39/1/008

[22] Szentgyorgyi, A. (1968) Bioelectronics: A Study in Cellular Regulations, Defense, and Cancer. Academy Press, New York.

[23] Szentgyorgyi, A. (1980) The Living State and Cancer. *Physiological Chemistry and Physics*, **12**, 99-110.

[24] Lorusso, G. and Rüegg, C. (2008) The Tumor Microenvironment and Its Contribution to Tumor Evolution Toward Metastasis. *Histochemistry and Cell Biology*, **130**, 1091-1103. https://doi.org/10.1007/s00418-008-0530-8

[25] Yang, M. and Brackenbury, W.J. (2013) Membrane Potential and Cancer Progression. *Frontiers in Physiology*, **4**, 185. https://doi.org/10.3389/fphys.2013.00185

[26] Szentgyorgyi, A. (1998) Electronic Biology and Cancer. Marcel Dekkerm, New York.

[27] Schwan, H.P. (1982) Nonthermal Cellular Effects of Electromagnetic Fields: AC-Field induced Ponderomotoric Forces. *British Journal of Cancer*, **45**, 220-224.

[28] Pething, R. (1979) Interfacial Dielectric Phenomena in Biological Systems in "Dielectric and Electronic Properties of Biological Materials". John Wiley & Sons Ltd., New York.

[29] Gabriel, C. (2006) Dielectric Properties of Biological Materials. In: Barnes, F.S. and Greenebaum, B., Eds., *Handbook of Biological Effects of Electromagnetic Fields*, CRC Press, Boca Raton, 52-95.

[30] Cole, K.S. (1968) Membranes, Ions and Impulses. University of California Press, Los Angeles.

[31] Pennock, B.E. and Schwan, H.P. (1969) Further Observations on the Electrical Properties of Hemoglobin-Bound Water. *The Journal of Physical Chemistry*, **73**, 2600-2610. https://doi.org/10.1021/j100842a024

[32] Schwan, H.P. (1963) Determination of Biological Impedances. *Physical Techniques in Biological Research*, **6**, 323-406. https://doi.org/10.1016/B978-1-4831-6743-5.50013-7

[33] Pliquett, F. and Pliquett, U. (1992) Tissue Impedance, Measured by Pulse Deformation. 8*th International Conference on Electrical Bio-Impedance*, Kuopio, 28-31 July 1992, 179-181.

[34] Loft, S.M., Conway, J. and Brown, B.H. (1992) Bioimpedance and Cancer Therapy. 8*th International Conference on Electrical Bio-Impedance*, Kuopio, 28-31 July 1992, 119-121.

[35] Pethig, R. (1984) Dielectric Properties of Biological Materials: Biophysical and Medical Applications. *IEEE Transactions on Electrical Insulation*, **19**, 453-474. https://doi.org/10.1109/TEI.1984.298769

[36] Bassingthwaighte, J.B., Leibovitch, L.S. and West, B.J. (1994) Fractal Physiology. Oxford University Press, Oxford.

[37] Zsoldos, I., Szendro, P., Watson, L. and Szasz, A. (2001) Topological Correlation in Amorphous Structures. *Computational Materials Science*, **20**, 28-36. https://doi.org/10.1016/S0927-0256(00)00120-8

[38] Vincze, Gy., Zsoldos, I. and Szasz, A. (2004) On the Aboav-Weaire Law. *Journal of Geometry and Physics*, **51**, 1-12. https://doi.org/10.1016/j.geomphys.2003.08.003

[39] Zsoldos, I. and Szasz, A. (1999) Appearance of Collectivity in Two-Dimensional Cellular Structures. *Computational Materials Science*, **15**, 441-448. https://doi.org/10.1016/S0927-0256(99)00031-2

[40] Maryan, M.I., Kikineshi, A.A. and Szasz, A. (2001) Self-Organizing Processes and Dissipative Structure Formation in the Non-Crystalline Materials. *Physics of the Solid State*, **2**, 585-593.

[41] Puck, T.T., Marcus, P.I. and Cieciura, S.J. (1956) Clonal Growth of Mammalian Cells *in Vitro*. *The Journal of Experimental Medicine*, **103**, 273-283. https://doi.org/10.1084/jem.103.2.273

[42] Taylor, A.F., Tinsley, M.R., Wang, F., Huang, Z. and Showalter, K. (2009) Dynamical Quorum Sensing and Synchronization in Large Populations of Chemical Oscillators. *Science*, **323**, 614-617. https://doi.org/10.1126/science.1166253

[43] Caer, G.L. (1991) Topological Models of Cellular Structures. *Journal of Physics A*: *Mathematical and General*, **24**, 1307-1317. https://doi.org/10.1088/0305-4470/24/6/022

[44] Puck, T.T. and Marcus, P.I. (1955) A Rapid Method for Viable Cell Titration and

Clone Production with Hela Cells in Tissue Culture: The Use of X-Irradiated Cells to Supply Conditioning Factors. *Proceedings of the National Academy of Sciences of the United States of America*, **41**, 432-437. https://doi.org/10.1073/pnas.41.7.432

[45] Camazine, S., Deneubourg, J.L., Franks, N.R., Sneyd, J., Theraula, G. and Bonabeau E. (2003) Self-Organization in Biological Systems. Princeton University Press, Princeton.

[46] Raff, M.C. (1992) Social Controls on Cell Survival and Cell Death. *Nature*, **356**, 397-400. https://doi.org/10.1038/356397a0

[47] Goldberger, A.L., Amaral, L.A.N., Hausdorff, J.M., Ivanov, P.Ch., Peng, C.K. and Stanley, H.E. (2002) Fractal Dynamics in Physiology: Alterations with Disease and Aging. *Proceedings of the National Academy of Sciences of the United States of America*, **99**, 2466-2472. https://doi.org/10.1073/pnas.012579499

[48] Szasz, A. (2015) Bioelectromagnetic Paradigm of Cancer Treatment Oncothermia. In: Rosch, P.J., Ed., *Bioelectromagnetic and Subtle Energy Medicine*, CRC Press, Boca Raton, 323-336.

[49] Vincze, G., Szasz, N. and Szasz, A. (2005) On the Thermal Noise Limit of Cellular Membranes. *Bioelectromagnetics*, **26**, 28-35. https://doi.org/10.1002/bem.20051

[50] Onsager, L. (1931) Reciprocal Relations in Irreversible Processes. I. *Physical Review*, **37**, 405-426. https://doi.org/10.1103/PhysRev.37.405

[51] Yablonsky, G.S., Gorban, A.N., Constales, D., Galvita, V.V. and Marin, G.B. (2011) Reciprocal Relations between Kinetic Curves. *Europhysics Letters*, **93**, 1-6. https://doi.org/10.1209/0295-5075/93/20004

[52] Szasz, A., Vincze, G., Szasz, O. and Szasz, N. (2003) An Energy Analysis of Extracellular Hyperthermia. *Electromagnetic Biology and Medicine*, **22**, 103-115. https://doi.org/10.1081/JBC-120024620

[53] Galeotti, T., Borrello, S., Minotti, G. and Masotti, L. (1986) Membrane Alterations in Cancer Cells: The Role of Oxy Radicals. *Annals of the New York Academy of Sciences*, **488**, 468-480.

[54] Sackmann, L.E. (1995) Handbook of Biological Physics. Elsevier, Amsterdam, 1.

[55] Andocs, G., Szasz, O. and Szasz, A. (2009) Oncothermia Treatment of Cancer: From the Laboratory to Clinic. *Electromagnetic Biology and Medicine*, **28**, 148-165. https://doi.org/10.1080/15368370902724633

[56] Yang, K.L., Huang, C.C., Chi, M.S., Chiang, H.C., Wang, Y.S., Andocs, G., Wang, H.E. and Chi, K.H. (2016) *In Vitro* Comparison of Conventional Hyperthermia and Modulated Electro-Hyperthermia. *Oncotarget*, **51**, 84082-84092.

[57] Andocs, G., Renner, H., Balogh, L., Fonyad, L., Jakab, C. and Szasz, A. (2009) Strong Synergy of Heat and Modulated Electromagnetic Field in Tumor Cell Killing. *Strahlentherapie und Onkologie*, **185**, 120-126. https://doi.org/10.1007/s00066-009-1903-1

[58] Tsang, Y.W., Huang, C.C., Yang, K.L., Chi, M.S., Chiang, H.C., Wang, Y.S., Andocs, G., Szasz, A., Li, W.T. and Chi, K.H. (2015) Improving Immunological Tumor Microenvironment Using Electro-Hyperthermia Followed by Dendritic Cell Immunotherapy. *BMC Cancer*, **15**, 708. https://doi.org/10.1186/s12885-015-1690-2

[59] Roussakow, S. (2017) Clinical and Economic Evaluation of Modulated Electrohyperthermia Concurrent to Dose-Dense Temozolomide 21/28 Days Regimen in the Treatment of Recurrent Glioblastoma: A Retrospective Analysis of a Two-Centre German Cohort Trial with Systematic Comparison and Effect-to-Treatment Analysis. *BMJ Open*, **7**, 1-34.

[60] Hager, E.D., Dziambor, H., Höhmann, D., Gallenbeck, D., Stephan, M. and Popa, C. (1999) Deep Hyperthermia with Radiofrequencies in Patients with Liver Metastases from Colorectal Cancer. *Anticancer Research*, **19**, 3403-3408.

[61] Gadaleta-Caldarola, G., Infusino, S., Galise, I., Ranieri, G., Vinciarelly, G., Fazio, V., Divella, R., Daniele, A., Filippelli, G. and Gadaleta, C.D. (2014) Sorafenib and Locoregional Deep Electro-Hyperthermia in Advanced Hepatocellular Carcinoma: A Phase II Study. *Oncology Letters*, **8**, 1783-1787. https://doi.org/10.3892/ol.2014.2376

[62] Szasz, A. (2014) Current Status of Oncothermia Therapy for Lung Cancer. *Korean Journal of Thoracic and Cardiovascular Surgery*, **47**, 77-93. https://doi.org/10.5090/kjtcs.2014.47.2.77

[63] Lee, D.Y., Haam, S.J., Kim, H.T., Lim, J.Y., Kim, E.J. and Kim, N.Y. (2013) Oncothermia with Chemotherapy in the Patients with Small Cell. *Lung Cancer*, **2013**, Article ID 910363.

[64] Lee, S.Y., Lee, N.R., Cho, D.H. and Kim, J.S. (2017) Treatment Outcome Analysis of Chemotherapy Combined with Modulated Electro-Hyperthermia Compared with Chemotherapy Alone for Recurrent Cervical Cancer, Following Irradiation. *Oncology Letters*, **14**, 73-78. https://doi.org/10.3892/ol.2017.6117

[65] Pang, C.L.K., Zhang, X., Wang, Z., Ou, J., Lu, Y., Chen, P., Zhao, C., Wang, X., Zhang, H. and Roussakow, S, (2017) Local Modulated Electro-Hyperthermia in Combination with Traditional Chinese Medicine vs. Intraperitoneal Chemoinfusion for the Treatment of Peritoneal Carcinomatosis with Malignant Ascites: A Phase II Randomized Trial. *Molecular and Clinical Oncology*, **6**, 723-732. https://doi.org/10.3892/mco.2017.1221

[66] Jeung, T.S., Ma, S.Y., Choi, J.H., Yu, J., Lee, S.Y. and Lim, S. (2015) Results of Oncothermia Combined with Operation, Chemotherapy and Radiation Therapy for Primary, Recurrent and Metastatic Sarcoma. *Case Reports in Clinical Medicine*, **4**, Article ID: 56280. https://doi.org/10.4236/crcm.2015.45033

[67] Volovat, C., Volovat, S.R., Scripcaru, V., Miron, L. and Lupascu, C. (2014) The Results of Combination of Ifosfamid and Locoregional Hyperthermia (EHY 2000) in Patients with Advanced Abdominal Soft-Tissue Sarcoma after Relapse of First Line Chemotherapy. *Romanian Reports in Physics*, **66**, 175-181.

[68] Volovat, C., Volovat, S.R., Scripcaru, V. and Miron, L. (2014) Second-Line Chemotherapy with Gemcitabine and Oxaliplatin in Combination with Loco-Regional Hyperthermia (EHY-2000) in Patients with Refrctory Metastatic Pancreatic Cancer-Preliminary Results of a Prospective Trial. *Romanian Reports in Physics*, **66**, 166-174.

[69] Dani, A., Varkonyi, A., Magyar, T. and Szasz, A. (2008) Clinical Study for Advanced Pancreas Cancer Treated by Oncothermia. *Forum Hyperthermie*, **1**, 13-20.

[70] Douwes, F.R. and Lieberman, S. (2002) Radiofrequency Transurethral Hyperthermia and Complete Androgen Blockade: A Nonsurgical Approach to Treating Prostate Cancer. *Alternative & Complementary Therapies*, **8**, 149-156. https://doi.org/10.1089/107628002760090994

[71] Douwes, F.R. (2001) Transurethral Hyperthermia in Early Stage Prostate Cancer. *Focus on Alternative and Complementary Therapies*, **6**, 77-78. https://doi.org/10.1111/j.2042-7166.2001.tb02809.x

Scientific Research Publishing

Open Journal of Biophysics, 2019, 9, 110-130
http://www.scirp.org/journal/ojbiphy
ISSN Online: 2164-5396
ISSN Print: 2164-5388

Spectroscopic Characterization of the Interaction between Dopamine and Human Serum Albumin

Imtiaz M. Khalid[1], Sawsan E. Abu Sharkh[2], Husain Samamarh[2], Rania Alfaqeeh[2], Musa M. Abuteir[2], Saqer M. Darwish[2]

[1]Department of Chemistry, Birzeit University, Birzeit, Palestine
[2]Department of Physics, Al Quds University, Beit Hanina, Abu Dis, al-Bireh, Palestine
Email: imtiazkhld@yahoo.com

How to cite this paper: Khalid, I.M., Abu Sharkh, S.E., Samamarh, H., Alfaqeeh, R., Abuteir, M.M. and Darwish, S.M. (2019) Spectroscopic Characterization of the Interaction between Dopamine and Human Serum Albumin. *Open Journal of Biophysics*, **9**, 110-130.
https://doi.org/10.4236/ojbiphy.2019.92009

Received: August 20, 2018
Accepted: February 24, 2019
Published: February 27, 2019

Abstract

The interactions of HSA with DA have received great attention nowadays due to its significant effect in the biomedical field and overall health. The main aim of this work is to examine the interaction between DA and HSA at physiological conditions. Upon addition of DA to HSA, the fluorescence emission was quenched with quenching constant $K_q = 1.32 \times 10^9$ $L \cdot mol^{-1} \cdot s^{-1}$ and the binding constant of DA with HSA is found to be $K = 4.4 \times 10^2$ mainly indicating dynamic quenching. The HSA conformation was altered upon binding of DA to HSA with an increase in α-helix and a decrease in β-sheets suggesting unfolding of HSA secondary structure due to weak intermolecular interaction with HSA. In view of the evidence presented, it is important to understand the details of the interactions of HSA with DA which will be crucial in the design of new DA-inspired drugs and help revealing vital details to better understand the HSA's role as a transporter for many drugs.

Keywords

Dopamine, HSA, Binding Constant, Non-Linear Stern-Volmer Plot, Protein Secondary Structure, FT-IR Spectroscopy

1. Introduction

Dopamine (DA), chemical structure provided in the top part of **Figure 1** [1], is a catecholamine neurotransmitter synthesized within the brain in the dopaminergic neurons and is involved in regulating multiple functions including movement and memory. DA transmits signals between neurons throughout human

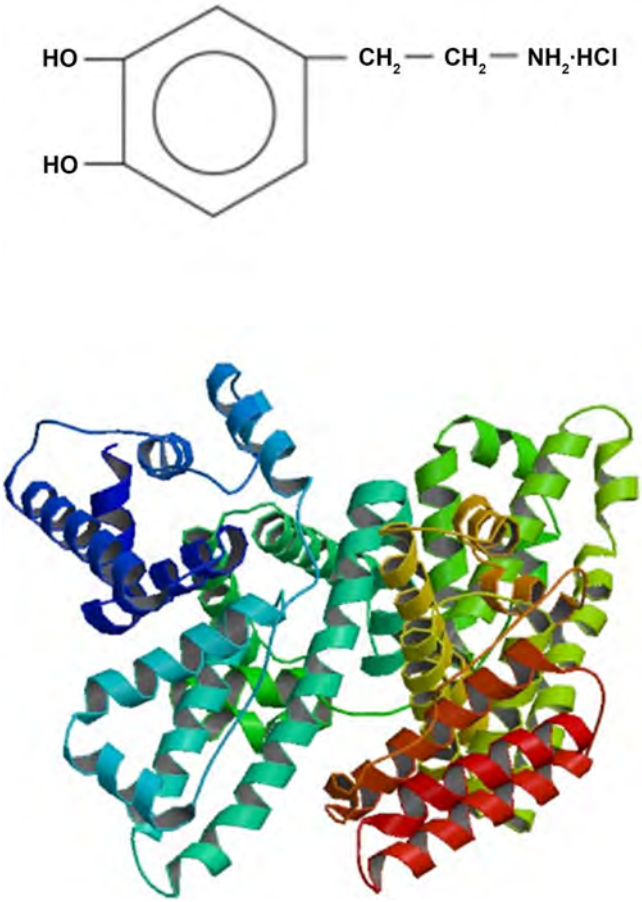

Figure 1. Chemical structure of dopamine hydrochloride (top). Secondary structure of HSA (bottom).

brain and body. The elevated or reduced dopamine level may cause memory loss related diseases, attention deficit, hyperactivity disorder, daydreaming and not being able to stay on task. Any changes in the levels of this vital neurotransmitter chemical have been proven to be related to several dopaminergic neurological diseases depending on the affected region in the brain [2] [3] [4] [5]. For example, neurocognitive disorders related to memory, attention, and problem-solving functions result from decline of DA in frontal lobes of the brain which controls the flow of information from other areas of the brain [6] [7] [8]. Therefore, DA is considered a major target for drug designing applied in the treatment of neurological diseases.

Inadequate DA levels due to the loss of DA-producing cells have been related Parkinson's disease which is associated with a loss in the ability of well controlled movements [9] [10] [11]. Despite the ongoing research to understand these devastating disorders, the sophisticated causes of dopaminergic cells' loss in Parkinson's disease are only partially understood.

1.1. Human Serum Albumin (HSA)

Human serum albumin (HSA), secondary structure provided in the bottom part

of **Figure 1** [12], is the most prominent protein in the human blood plasma and it constitutes about 60% of the total plasma proteins. It is a single-chain polypeptide consisting of 585 amino acids residues stabilized by 17 disulfide bridges and has a molecular mass of 66.5 kDa. HSA high importance is due to its many important physiological functions [13] [14]. HSA is made up of three similar structural domains I, II, and III. Each domain is further divided into subdomain A and B. It is well documented that subdomains IIA and IIIA are known as the major drug binding sites for the majority of heterocyclic and aromatic compounds [12] [13]. Recent investigation has demonstrated the capacity of subdomain IB in binding drugs making it a potential for various drugs delivery [15]. These binding sites empower the HSA with an exceptional ability in binding various ligands, which adds to its biological importance in delivering number of drugs in the blood system to their targeting organs/tissues within the human body [16] [17]. Generally, HSA binds reversibly with wide range of drugs however some drugs with high affinity for HSA limit the drug distribution—of free form and the bound form—as well as the elimination of the drugs. In addition, the HAS-drug interactions play an important role in understanding the efficiency of the drug as determined by the free fraction of the drug [18] [19].

1.2. Alzheimer's Disease (AD)

AD, affecting millions of individuals worldwide, is an irreversible neurodegenerative disorder characterized by progressive cognitive decline and dementia [20]. The decline in cognitive function affects recent memory first then slowly spreads to other regions of the brain. As of now, the exact cause of AD is not known and currently there is no cure for this devastating disease. Therefore, any available treatment is meant to slow the progression of AD and relieves its symptoms. It has been suggested and well documented that AD originates in the brain [21] but a recent investigation have indicated that AD could have been triggered by breakdowns elsewhere in the body. This finding makes is promising in preventing AD from reaching the brain if proper drug targets the toxin protein and removes it while in the blood without the need to act directly on the brain, which is a very challenging task to accomplish and hard-to-reach target safely [22] [23]. In addition, electrical signaling responsible for learning and memory is usually diminished in people with AD [24].

1.3. Parkinson's Disease (PD)

PD, a neurological disorder that affects movement control, neurons progressively degenerate and as a result, the amount of DA available for neurotransmission in the brain is lowered [25] [26]. The main symptoms of PD due to DA imbalance include resting tremor, rigidity, a gradual slowness of natural movement, poor balance and diminished motor coordination [9] [27].

The underlying cause of PD is the progressive loss of dopaminergic neurons in some neurons and the presence of Lewy bodies—abnormal protein aggregates—in the remaining neurons [24]. The neural loss leads to dopamine defi-

ciency which is believed to be responsible neurodegenerative "motor disease". The main therapy to treat PD is by dopamine replacement merely relieves the associated symptoms but the disease continues its progression. Therefore, there is a need for understanding the process of the neurological degeneration to develop effective drugs to stop the degeneration [10] [11].

In addition to PD, alterations in the dopamine levels have been consistently observed and reported in AD patients, including lower levels of dopamine (DA) [28] [29]. Although research investigations have resulted in developing few theories about AD, until now there is no definite reason standing out as the cause of this disturbing disease [21] [30] [31]. There is evidence supporting the conception that dopaminergic system dysfunction has a role in cognitive decline symptoms of AD, however, the cause of dopaminergic system dysfunction in AD remains to be elucidated [2] [24] [32].

Drug binding to HSA plays a major role in the drug efficacy—the ability of a drug to provide a beneficial effect—which is affected by drug distribution—the process of delivering a drug from the plasma to the tissue(s) where the drug's actions are needed. Most of the drugs used by humans are bound to HSA which influences the drug distribution, absorption and efficiency [15] [16] [17] [18] [19] [33] [34] [35]. Since dopamine is recognized for its high pharmaceutical value as a potential candidate for treatment of neurological disorders such as AD and PD [8] [36] and it's binding to HSA is not quite understood, therefore, the interaction of dopamine, a potential drug, with HSA is highly important to better understand the drug-protein complex in terms of structural changes and stability to better elucidate its pharmacological importance. Therefore, the interaction of dopamine and HSA is crucial to better understand the HSA-DA complexation, provide significant information about HSA-DA stability as a complex, and underline the role of HSA in delivering DA to the blood stream. Similar to previous investigations with various other drugs [37] [38], this endeavor is fueled by spectroscopic characterization to investigate the interaction between the HSA and DA and determine the complex stability associated with this binding. To reach this, we used fluorescence in combination with UV absorption spectroscopy and Fourier transform infrared (FTIR) spectroscopy to study the interaction of DA with HSA to characterize the effect of this drug on HSA conformational changes resulting from such complex. FTIR spectroscopy is reliable in monitoring conformational changes when proteins interact with drugs due to detection of functional groups' changes due to interactions between the drug and the HSA thus affecting the overall secondary structure of the protein. Similar to other chemical compound, proteins have amide groups with the general structure of (—C(=O)−N—) which are clearly detected by FTIR. Therefore, any changes resulting from stabilization effects due to intermolecular forces, will cause changes to vibrational modes of the amide groups of the proteins. Similarly, fluorescence spectroscopy is a powerful analytical chemistry technique in providing structural changes information due to quenching upon intermolecular

forces. Thus, fluorescence contributes in providing data to calculate binding constants and binding sites.

2. Experimental

2.1. Samples' Preparations and Materials

HSA protein (66,500 Da) and dopamine (189.2 g/mol) in powder form were purchased from Sigma Aldrich chemical company and were used without any further purifications. HSA stock solution was prepared in a concentration of 80 mg/ml dissolved in phosphate buffered saline with pH of 7.4 which corresponds to 1.2 mM. The final concentration of HSA in the HSA-DA complex was 40 mg/ml equivalent to molarity of 0.6 mM which is comparable to its concentration in the blood [15].

Dopamine stock solution with molarity of 4.8 mM, was prepared by dissolving dopamine hydrochloride in enough distilled water to prepare DA stock solution.

DA standard solutions were prepared by successive dilutions. The HSA-DA complexes were prepared by mixing equal volumes of 1.2 mM HSA molarity and each of the standard DA solutions. The final concentration of HSA was kept at (40 mg/ml) in all samples while the concentrations of dopamine in the final HSA dopamine solutions was reduced to be as (0.15 mM, 0.3 mM, 0.4 mM, 0.5 mM, 0.6 mM, 1.0 mM, 1.2 mM and 2.4 mM).

2.2. Thin Film Preparation

Silicon windows (NICODOM Ltd.) were used as spectroscopic cell window. 60 μl of each sample of HSA-DA was spread on silicon window using spincoater to obtain equal thickness of each sample, then incubator was used to evaporate the solvent to obtain transparent thin film on the silicon window. All solutions were prepared at the same time at room temperature and were stored under the same conditions.

3. Instrumentation

3.1. FT-IR Spectroscopic Measurements

The FT-IR measurements were obtained used Bruker IFS 66/S spectrophotometer equipped with a liquid nitrogen-cooled MCT detector and KBr beam splitter. Silicon windows (NICODOM Ltd) were used as spectroscopic cell windows. Complexes' solutions (0.15, 0.3, 0.6, 0.7, 0.9) mM were prepared at room temperature. 60 μL of each sample of HSA-DA was spread on silicon window using spin coater to obtain equal thickness of each sample, and then was incubated for two hours to evaporate the solvent in order to obtain transparent thin film on the silicon window. The spectrophotometer was continuously purged with dry air during the measurements. The absorption spectra were obtained in the range of (400 - 4000) cm^{-1}. A spectrum was taken as an average of 60 scans to enhance the signal to noise ratio, and the spectral resolution was at 4 cm^{-1}. The aperture used in this study was 8 mm, since it gave the best signal to noise ratio. Baseline

correction, normalization and peak areas calculations were performed for all the spectra by OPUS software. The peak positions were determined using the second derivative of the spectra. The infrared spectra of HSA and the HSA-DA complexes were obtained in the region of (1200 - 1700) cm^{-1}. The FTIR spectrum of free HSA was acquired by subtracting the absorption spectrum of the buffer solution from the spectrum of the protein solution. For the net interaction effect, the difference spectra {(HSA-DA) - (HSA)} were generated using the featureless region of the spectra at (1800 - 2200) cm^{-1}.

3.2. UV-VIS Absorption Spectra

The data was collected using 5 μL samples using NanoDrop ND-1000 Spectrophotometer for the free HSA (40 mg/ml or 0.6 mM) and for the HSA-DA complexes solutions with the following concentrations (0.15, 0.3, 0.4, 0.5, 0.6, 1.0, 1.2, and 2.4) mM. UV measurements were repeated for all the samples and no significant differences were observed. The UV-absorption spectra of HSA-DA complex are obtained at the wavelength of 280 nm.

3.3. Fluorescence

The fluorescence measurements were obtained using NanoDrop ND-3300 Fluorospectometer for the following complexes concentration (0.15, 0.3, 0.4, 0.5, 0.6, 1.0, 1.2, and 2.4) mM at 25˚C. The excitation source comes from one of three solid-state light emitting diodes (LEDs) including UV LED with maximum excitation 365 nm, Blue LED with excitation 470 nm, and white LED from 500 to 650 nm excitation. A 2048-element CCD array detector covering 400 - 750 nm, is connected by an optical fibre to the optical measurement surface. The excitation is done at the wavelength of 360 nm and the maximum emission wavelength is at 440 nm.

4. Results

4.1. UV-Absorption Spectroscopy

The UV absorbance spectra of different concentration of dopamine with a fixed concentration of HSA which were scanned over a range of 220 - 350 nm are presented in **Figure 2**. Each spectrum indicates two absorption maximum wavelengths at about 230 and 280 nm. The figure shows direct relationship between the increase in peak intensity of the HSA-DA complex and the concentration of the DA. This increase in intensity is due to interaction between HSA and DA as monitored in buffered solution by scanning the wavelengths. As indicated in the figure, there is a clear absorption signal for free DA.

The reciprocal plot of $1/(A - A_o)$ versus $(1/l)$ is linear as indicated in **Figure 3**. When a fixed concentration of *HSA* was allowed to complex with various amounts of *DA*, there is a linear increase in the UV absorbance of *HSA*. A binding constant for the HSA-DA complex was calculated using UV spectra according to published methods [16] with the assumption that there is one-to-one

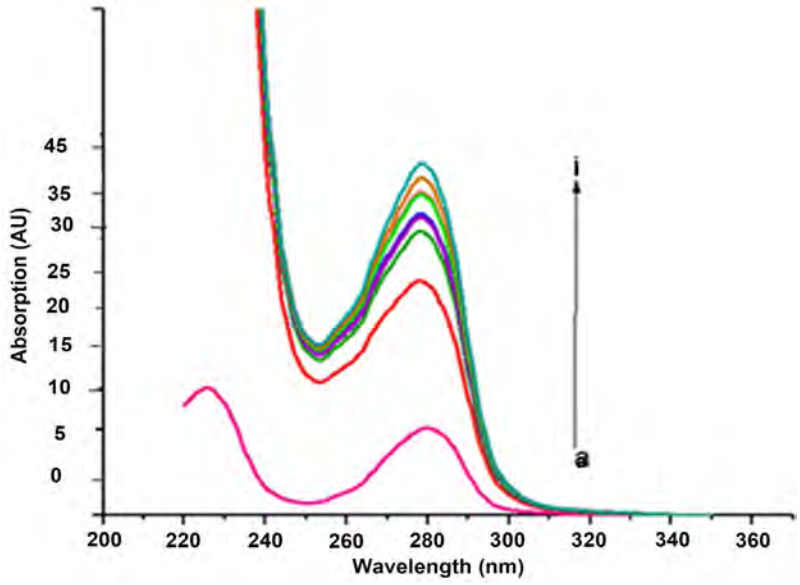

Figure 2. UV absorbance spectra of HSA-DA in 0.1 M PBS with pH 7.4 at 25˚C. Free HSA (40 mg/mL, 0.6 mM) and free HSA with different DA concentrations (a = free DA (4.8 mM), b = free HSA (0.6 mM), c-i correspond to HSA-DA complexes with (0. 3, 0.4, 0.5, 0.6, 1.0, 1.2 and 2.4) mM DA respectively.

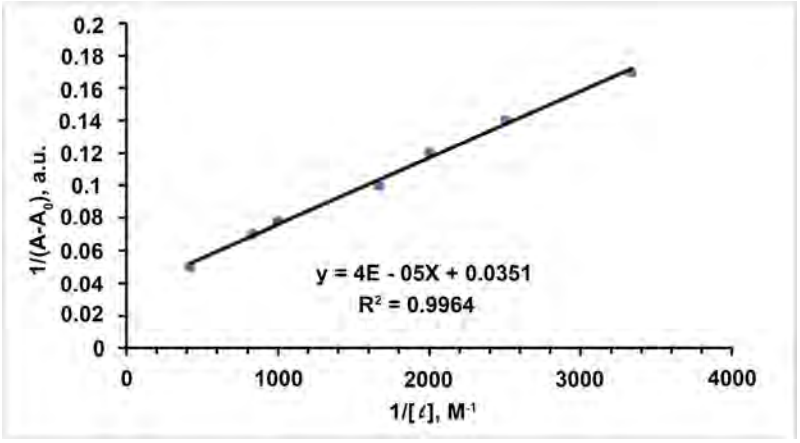

Figure 3. The plot of $1/(A-A_0)$ vs. $1/l$ for free HSA (40 mg/mL, 0.6 mM) and with different HSA-DA complex concentrations in 0.1 M PBS with pH 7.4.

interaction between *HSA* and *DA* in aqueous solution to establish chemical equilibrium as in the following equation.

$$HSA + DA \leftrightarrow HSA : DA \tag{1}$$

The corresponding formation/binding constant:

$$K = [HSA : DA] / [DA][HSA] \tag{2}$$

on the following equation.

$$1/(A - A_0) = 1/(A - A_0) + 1/k(A_\infty - A_0) * 1/l \tag{3}$$

where A_o corresponds to the initial absorption of *HSA* at 280 nm in the absence of *DA*, A_∞ is the final absorption of the *HSA*, and *A* is the recorded absorption at

different *DA* concentration (*I*).

The binding constant (*K*) for HSA-DA complex was estimated from the ratio of the intercept to the slope and was found to be 8.54×10^2 M^{-1}. The value for the binding constant is an indication of a weak intermolecular force interaction between the HSA and DA when compared to reported HSA-drug interaction with binding constant in the range of 10^4 and 10^6 M^{-1} [39] The importance of the binding constant value stems from its valuable application in drug delivery and pharmacokinetics [17] therefore, absorbance measurements were constantly repeated and similar results were obtained consistently. In addition, absorbance spectra were recorded for DA free with various concentrations corresponding to those of DA concentrations in the final HSA-DA complex. To further investigate the nature of the complexation-interaction, the absorbance value from the spectra of free HSA was added to the absorbance value of the free HSA at 280 nm. The corresponding added absorbances' values clearly indicate that the signal obtained for the various individual added concentrations of the free HSA and free DA are comparable in magnitude to those of HSA-DA complex with same final concentration. This result supports the speculation that the interaction between HSA and DA is weak interaction.

4.2. Fluorescence Emission Spectroscopy

The emission spectra in the range of 400 to 750 nm were obtained for HSA-DA spectra are shown in **Figure 4**. When a fixed concentration of HSA is titrated with various amounts of DA, a decrease in the fluorescence emission of HSA is clearly presented. The quenching took place in a concentration dependent manner; an increase in DA concentration led to decrease in HSA fluorescence intensity. It is well established that HSA fluorescence is mainly due to Tryptophan (Trp), which is located at 214 position of subdomain IIA with very minor contribution from tyrosine (Try) and phenylalanine which provide very low quantum yields and therefore can be ignored [19] As a result, the fluorescence quenching is caused by addition of different concentrations of DA which causes quenching of fluorescence emission. This quenching could be a result of DA binding to HSA – a major drug carrier protein in the human blood plasma. Another reason is the possibility of formation of HSA-DA complex. There is no noticeable peak positional shift indicating that no major structural alternations of HSA upon binding with DA. Peak shifts, appearance of new peaks, disappearance of existing peaks or various combinations of the mentioned are main characteristic of major structural changes.

The HSA fluorescence is decreased upon increasing concentrations of DA, which indicates that the DA is interacting with HSA in the surrounding of the HSA main fluorescent residue Trp214 in subdomain IIA. The interaction between the DA and HSA can affect HSA fluorescence upon binding to DA due to the quenching ability of a tryptophan residue upon colliding with DA. Careful examination of the absorption spectra does not show and major changes and

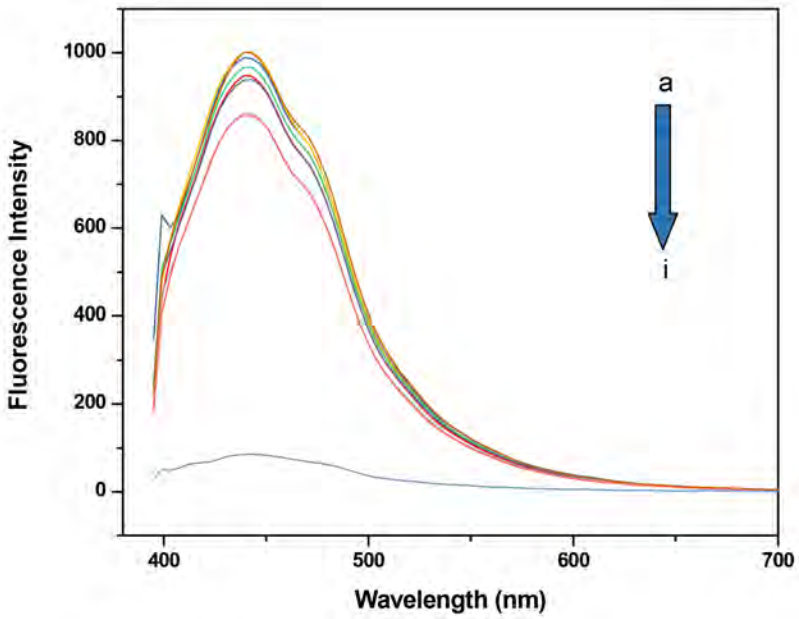

Figure 4. Fluorescence emission spectra of free HSA and HSA-DA in 0.1 M PBS with pH 7.4, λex = 360 nm, λem = 439 and temperature at 25˚C. a = Free HSA (40 mg/mL, 0.6 mM), *i* = free DA (4.8 mM), and (b-h) correspond to HSA with different DA concentrations (b = 0. 3, 0.4, 0.5, 0.6, 1.0, 1.2, and 2.4) mM DA.

very little changes is observed on the absorption spectra of the HSA shape as the DA concentration is added which is an indication of minor conformational changes due to collisional quenching [40].

Further, to elucidate the nature of the quenching mechanism as static or dynamic in the HSA-DA system, Stern-Volmer equation [35] is used to plot F_o/F versus l and the result is shown in **Figure 5**. The Stern-Volmer plot is non-linear, indicating that both types of static and dynamic quenching occur. HSA is quenched both by collisions and by complex formation with DA. Hence,

$$F_0/F = \left(1+K_{sv}\left[DA\right]\right)*\left(1+K_D\left[DA\right]\right) \quad (4)$$

where F and F_0 are the fluorescence intensities with and without quencher, K_D is the dynamic quenching constant of the biomolecule and K_{sv} is the Stern-Volmer quenching constant due to static quenching. This modified second order form of the Stern-Volmer equation with respect to DA concentration, accounts for the both static and dynamic quenching occur for the same fluorophore. When quenching is due to static quenching, the second parenthesis in Equation (4) is ignored and when the quenching is dynamic the first parenthesis is ignored. However, when both static and dynamic quenching are present, one must account for each type.

Fluorescence quenching can be induced by different mechanisms, which are usually classified into dynamic and static quenching. Dynamic quenching arises from collisional encounters between the fluorophore and quencher, and static quenching resulting from the formation of a ground state complex between the fluorophore and the quencher [40].

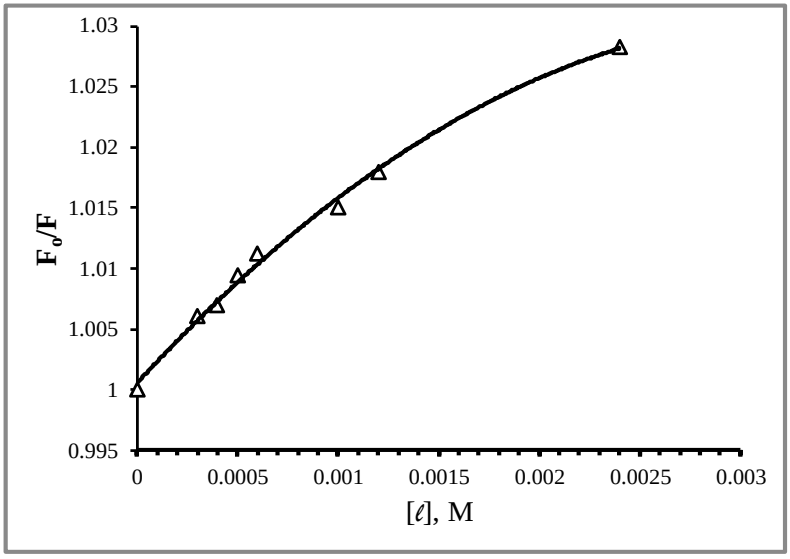

Figure 5. The Stern-Volmer plot for HSA-DA complexes.

To further understand the nature of quenching, the quadratic equation was solved using Excel for the K_D and K_{SV} values which were found to be $K_D = K_{SV} = 6.60\ M^{-1}$.

Using calculated K_D value of 6.6 M^{-1} and τ_0 as 5×10^{-9} s for HSA [40] which is typical for diffusion controlled reaction, the quenching constant, k_q, is calculated from the $k_{sv} = k_q \tau_0$ relation according to Stern-Volmer equation and which is determined to 1.32×10^9 $L{\cdot}mol^{-1}{\cdot}s^{-1}$ which is about the same as for collisional dynamic quenching constant for various quenchers with biopolymer (maximum value of 2×10^{10} $L{\cdot}mol^{-1}{\cdot}s^{-1}$) [12] [13]. This result implies that quenching is mainly due to dynamic collision and not to complex formation, but rather a dynamic quenching is mainly dominated [40] [41].

4.3. Accessibility of Tryptophan in HSA to Quenching by DA Using Fluorescence

When dynamic collisional quenching dominates as quenching type of fluorescence for HSA with drugs, it usually results in deviation from linearity of Stern-Volmer plots. Therefore, it becomes necessary to further analyze the non-linear Stern-Volmer plots to determine if the quenching is purely collisional and to determine the accessibility fluorophores. Hence the following modified Stern-Volmer can be used: [40].

$$F_0/F = \left(1/f_a K_a\right) * \left(1/[DA]\right) + \left(1/f_a\right) \tag{5}$$

where ΔF is the difference between the unquenched fluorescence and the quenched fluorescence, f_a is the fraction of the initial fluorescence that is accessible to quencher, K_a is the Stern-Volmer quenching constant of the accessible fraction, and $[DA]$ is the dopamine concentration. The K_a can be calculated from the slope of the straight-line equation resulting from plotting $F_0/(\Delta F)$ vs. $1/[DA]$ as shown in **Figure 6**. The obtained value of effective binding constant,

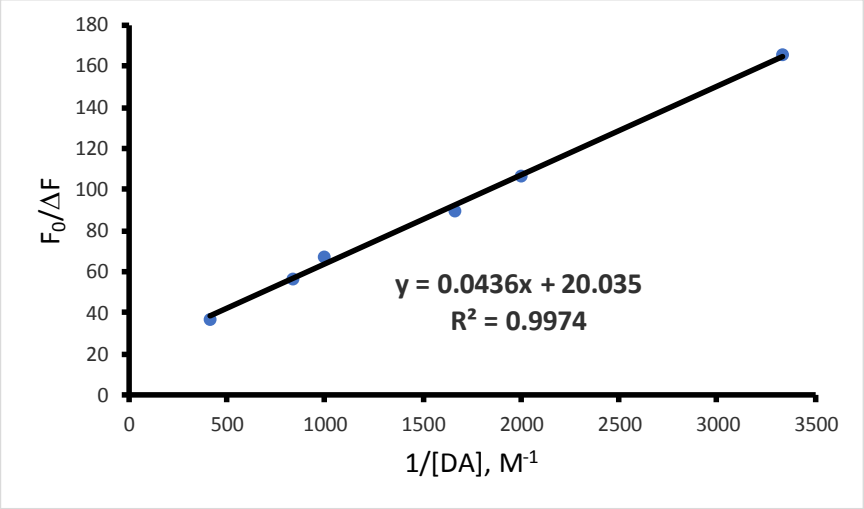

Figure 6. Modified Stern-Volmer plot for HSA-DA complexes for accessibility determination.

K_a is determined to be determined to be 4.4 × 102 M^{-1} and the accessible fraction f_a = 0.05 indicating that the Trp214 is not accessible for biding with DA which is in agreement with the small effective binding constant.

4.4. FT-IR Spectroscopy

FT-IR is used widely to analyze IR bands of structural characterization of proteins and provide clear information of any changes might occur due to various changes leading to decrease/increase in intensities of the original peaks as well as any shifts (blue/red due to interaction and or structural changes). HSA shows number of amide bands due to vibrations of various peptides within the protein. [42] Specifically, the amide groups of the peptides represent characteristic vibrational modes (amide modes) which are sensitive to protein structures and any incurred changes might cause structural changes. IR spectral data for the HSA give rise to nine characteristic IR absorption bands, namely, amide A, B, and I-VII [43] [44] [45].

Amide I band ranges from 1700 to 1600 cm^{-1} and is mainly due to C=O stretching vibrations of the peptide linkages. Amide II in the range of 1600 - 1480 cm^{-1} is due to the coupling of the N—H in-plane bending to C—N stretching vibration, while amide III band ranging from 1330 to 1220 cm^{-1} is due to the C—N stretching mode coupled to the in-plane N—H bending mode [45].

The FT-IR absorption spectra in the region of (1800 - 1200) cm^{-1} are shown in **Figure 7** for HSA and various HSA-DA complexes while HSA second derivatives are shown in **Figure 7** for free HSA (bottom) and HSA-DA complexes (top) while the difference spectra corresponding to free HSA and HSA-DA complex with various DA concentrations are shown in **Figure 8**. In addition, band assignments for the same spectra are presented in **Table 1** according to region and DA concentrations. The second derivative of free HSA is shown in

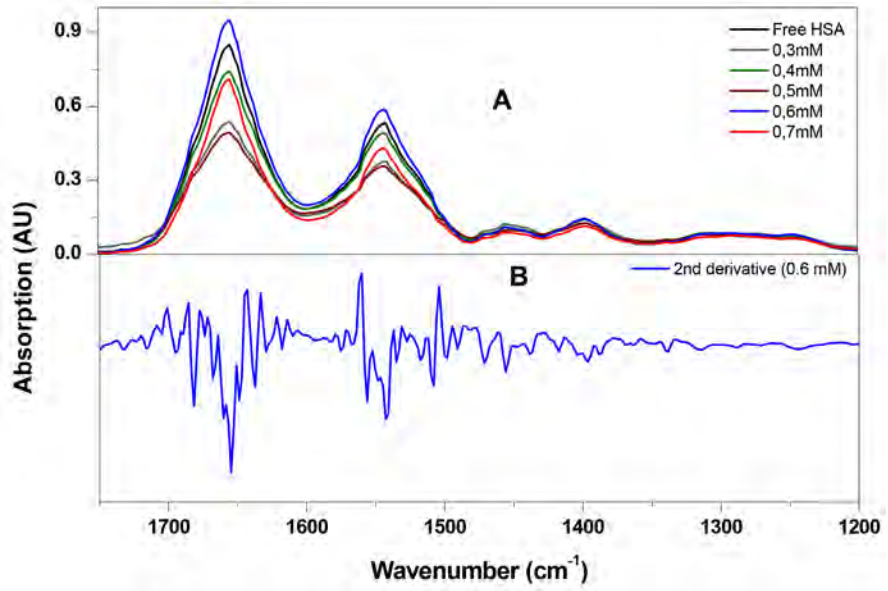

Figure 7. The FT-IR spectrum of 0.6 mM HSA free (bottom) and the spectra (second derivative) of DA-HSA complex (top) (a-f). DA concentration of 0.0 mM, 0.3 mM, 0.4 mM, 0.5 mM, 0.6 mM and 0.7 mM.

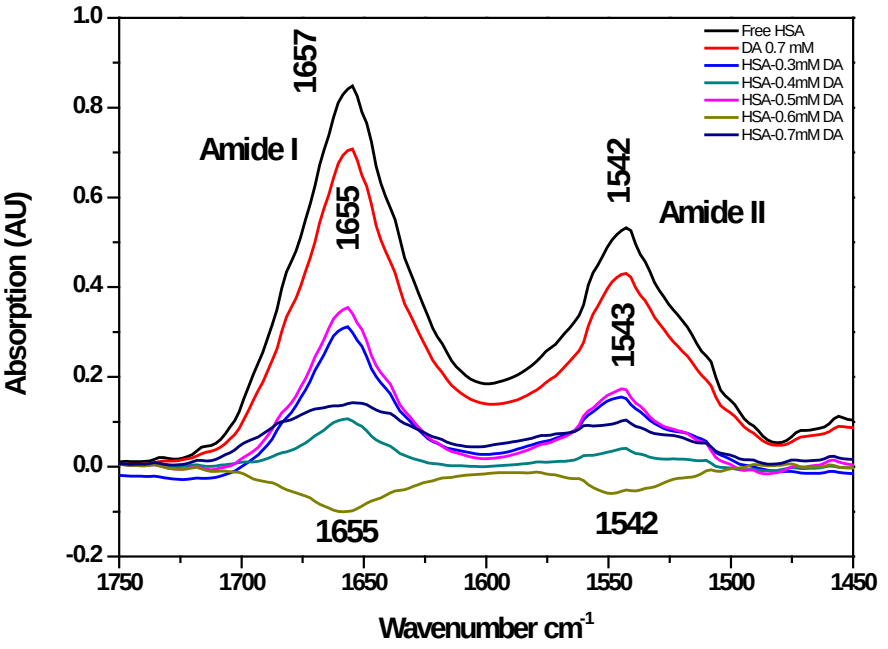

Figure 8. FT-IR spectra (top two curves, a (HSA free) and b (HSA + 0.7 mM DA) and differences spectra of HSA free and various DA-HSA complexes (c, d, e, f and g) with concentration of (0.3 mM, 0.4 mM, 0.5 mM, 0.6 mM and 0.7 mM).

Figure 8 (bottom) where the spectra is dominated by absorbance bands of amide I and amide II at 1655 cm^{-1} 1540 cm^{-1} respectively. It is clear from the figure that as the DA concentration increases, the intensity of the 1655 cm^{-1} 1540 cm^{-1} peaks decrease.

For DA-HSA interaction, the amide bands of HSA infrared spectra over all

Table 1. absorption peak assignment (in wavenumbers, cm^{-1}) for HSA-DA at different concentration.

Bands	**Range (cm^{-1})**	Free HSA	DA concentrations				
Amide I	**1700 - 1600**	**0.0**	**0.3 mM**	**0.4 mM**	**0.5 mM**	**0.6 mM**	**0.7 mM**
	β-sheets	1609	---	1609	---	1610	1610
	β-sheets	1622	1621	1622	1622	1623	1623
	Random	1636	1636	1636	1636	1636	1636
	α-helix	1656	1654	1655	1655	1655	1655
	Turns	1681	1681	1681	1680	1680	1681
	β-sheets	1695	1695	1695	1695	1695	1695
Amide II	**1600 - 1480**						
	β-sheets	1493	1494	1494	1495	1495	1494
	Random	1520	1523	1521	1523	---	---
	α-helix	1540	1542	1543	1543	1544	1544
	Turn	1574	1575	1576	1576	1575	1575
	β-sheets	1592	1594	1593	1593	1593	1593
Amide III	**1320 - 1220**						
	β-sheets	1231	1231	1231	1231	1231	1231
	β-sheets	1245	1245	1245	1245	1245	1245
	Random	1268	1271	1268	1267	1270	1268
	turn	1294	1293	1293	1293	1291	1290
	α-helix	1310	1309	1310	1310	1310	1310

shift is listed clearly in Table 1. In amide I band, the peak positions have shifted from the HSA free to HSA-DA after addition of 0.7 mM DA as follows: 1622 → 1623 cm^{-1}, 1656 → 1654 cm^{-1}, 1681 → 1680 cm^{-1}. In addition, the peak at 1609 cm^{-1} was fluctuating disappearing and appearing at various concentrations as shown in the table. For amide II, the peak positions have shifted as follow: 1493 → 1494 cm^{-1}, 1520 → 1523 cm^{-1} and disappeared at the last two highest DA concentration, 1540→ 1544 cm^{-1}, 1574 → 1575 cm^{-1} and 1592 → 1593 cm^{-1}. In amide III region, the only peak shift is on: 1294 → 1290 cm^{-1}.

The 1656 cm^{-1} and 1540 cm^{-1}, which correspond to amide I and amide II, respectively represent the location of both the amide bonds orientation are sensitive to the HSA secondary structure because both groups of C=O and the N-H bonds are involved in the hydrogen bonding that takes place between the different elements of secondary structure [17] [46]. The overall change in peaks positions indicate HSA secondary structural changes due to interaction with DA. This shift in peak positions is mainly contributed to collisional electrostatic interaction between the HSA and the DA. Shifts to lower wavenumbers for the major peak in amide I *i.e.* 1656 → 1654 cm^{-1} is mainly due to stabilization by intermolecular interaction between the non-bonding pair of electrons on the oxy-

gen of the carbonyl C=O and the hydrogen of N—H thus causing the corresponding amide II shift from 1540 to 1544 cm^{-1}. Looking at the overall data in Table 1, it is obvious that the peak change (appearance, disappearance or shift) was stabilized or reached a steady behavior when the ratio of DA to HSA was approaching 1, specifically when the DA concentration reached 0.6 mM which corresponds to 1:1 ratio with the HSA and beyond.

FT-IR spectra for the HSA-DA interaction are shown in Figure 8. The FT-IR spectra (top two curves) and difference spectra {HSA-DA complex—HSA free} for HSA-DA different ratios complexes in amide I and amide II regions are clearly presented. There is no appearance of any new peaks or major shift in peak position. However, in amide I region, there is a negative peak at 1655 cm^{-1} with little shift of position that increases in intensity as the DA concentration is increased which corresponds to increase in HSA-DA complex concentration. Similar behavior is noted in amide II region with a negative feature at 1542 cm^{-1}. The negative peaks behavior is attributed to the change in intensity of amide I and II bands which is a result of change of the secondary structure of HSA after combination with DA due to intermolecular interaction between the DA and the C=O and or N—H groups [46] [47].

The component bands of three amide regions, I, II and III were attributed according to the well-established principle [48] [49] as follows: the bands in the range of 1610 - 1640 cm^{-1} are generally assigned to -sheet, bands in the range 1640 - 1650 cm^{-1} correspond to random coil, bands in the range 1650 - 1658 cm^{-1} are attributed to α-helix and the 1660 - 1700 cm^{-1} bands correspond to β-turn structure. The absorption bands in amide II consist of four components assigned in the following order: 1488 - 1500 cm^{-1} to β-sheets, 1504 - 1525 cm^{-1} to random coil, 1527 - 1560 cm^{-1} to α-helix and 1564 - 1585 cm^{-1} to turn structure. The component bands of amide III have been assigned as follows: 1330 - 1290 cm^{-1} to α-helix, 1290 - 1270 cm^{-1} to β-turn and 1220 - 1250 cm^{-1} to β-sheets. Percentage determination of the contribution of each secondary structural element in the HSA-DA complex secondary structure was carried out based on the assignment criterion for each of the HSA free and after the interaction with DA in amides I, II, and III. The quantitative analysis of the HSA was performed to determine any change in the secondary structure of HSA due to complexation with DA.

The components bands of amide I, II, and III regions were assigned using Fourier self-deconvolution (FSD) and second derivative resolution with curve fitting as shown in Figure 9.

For amide I band, the components are assigned as follows: 1606 - 1620 cm^{-1} represent β-sheet, 1620 - 1647 cm^{-1} represent random coil, 1649 to 1670 cm^{-1} correspond to α-helix, 1672 - 1687 cm^{-1} to turn structure and 1687 - 1700 cm^{-1} correspond to β-antiparallel. For amide II region, the absorption bands are assigned in the following order: 1487-1506 cm^{-1} to β-sheet, 1506 - 1523 cm^{-1} to random coil, 1523 - 1558 cm^{-1} to α-helix, 1560 - 1585 cm^{-1} to turn structure and 1585 - 1600 cm^{-1} to β-antiparallel. For amide III region, the bands are assigned

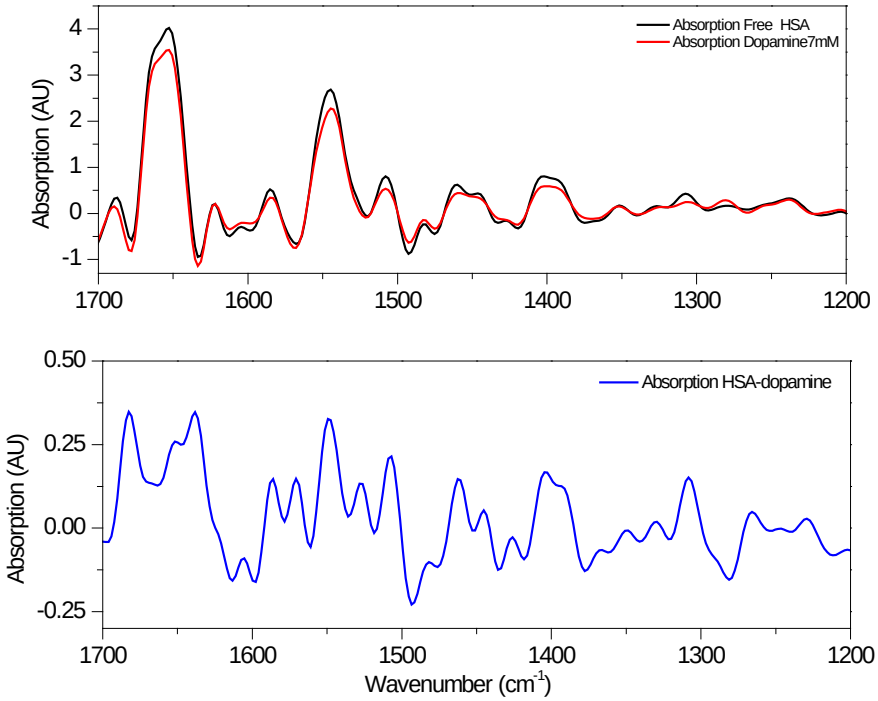

Figure 9. Fourier self-deconvolutions (FSD) spectra subtraction: top {free HSA - HSA-DA (0.7 mM)}, bottom the final result of the subtraction.

as follows: 1220 - 1256 cm^{-1} to β-sheet, 1259 - 1287 cm^{-1} to random coil, 1288 - 1302 cm^{-1} to turn structure, and 1302 - 1331 cm^{-1} to α-helix. Most investigations have revealed that amid I bands are most sensitive in contributing to the secondary structure change however many studies reported informational contribution from amide II and III and can be used to study the secondary structure of protein. [50] [51] [52].

In this work, the percentage of each secondary element of HSA secondary structure were calculated using normalization to integrate areas of the components bands in amide I, II, and III divided by the total area. The obtained values represent relative intensities for each of the secondary element with the specified region while the area under each secondary element corresponds to its percentage. **Figure 10** shows the percentages determination for the secondary structure of HSA in amide I region. Similar figures were obtained for each of amide II and amide III regions. The obtained data in **Table 2** is extracted from **Figure 10** and curve-fitted for amide I, II and III regions and secondary structure determinations of the HSA free and its DA various complexes in dehydrated films. The table clearly lists the percentages of each secondary structure of HSA before and after the interaction with DA at different concentration. As a general trend, as DA concentrations are increased, α-helix percentage increased in the three amide regions which is accompanied by overall decrease β-sheet percentages in the same regions.

The increase in α-helix percentage and the decrease in β-sheets are believed to be due to the unfolding of the HSA in the presence of DA because of weak

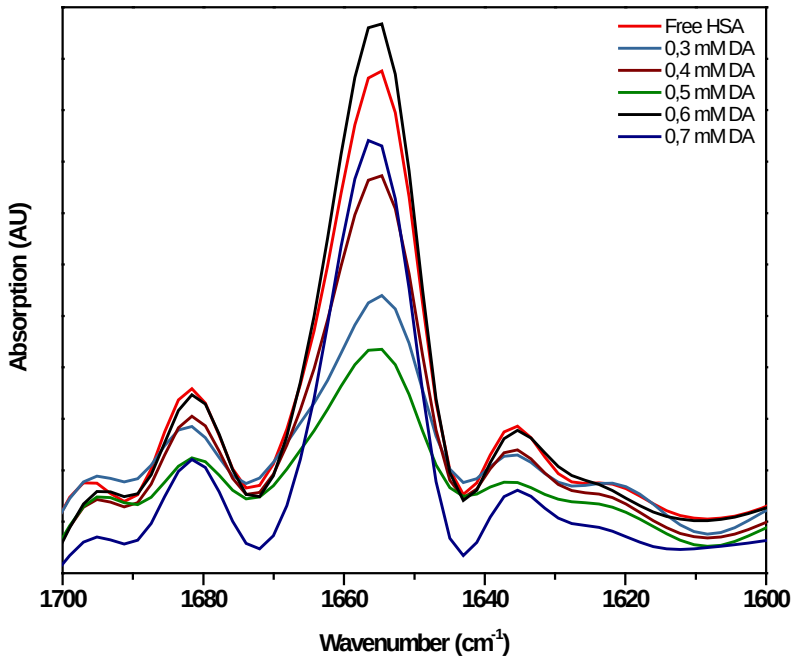

Figure 10. Deconvolution curve for determination the percentages for secondary structure of HSA in amide I.

Table 2. Secondary structure determination for amide I, amide II, and amide III regions for HSA free and HSA-DA complexes.

Bands	Range (cm^{-1})	Intensity %	Intensity %	Intensity %	Intensity %	Intensity %	Intensity %
		Free HSA	0.3 mM	0.4 mM	0.5 mM	0.6 mM	0.7 mM
Amide I				1700 - 1600 (cm^{-1})			
β-sheets	1614 - 1628	3	5	3	3	1	1
Random	1628 - 1643	12	11	11	9	11	11
α-helix	1645 - 1672	65	56	65	55	68	70
Turns	1674 - 1687	13	14	13	16	12	11
β-sheets (Anti)	1689 - 1700	7	14	8	17	8	7
Amide II				1600 - 1480 (cm^{-1})			
β-sheets	1484 - 1500	7	6	5	6	6	6
Random	1502 - 1531	25	19	17	13	18	19
α-helix	1533- 1564	22	20	32	26	32	34
Turns	1564 - 1585	19	20	18	18	18	18
β-sheets anti	1585 - 1600	27	35	28	37	26	23
Amide III				1320 - 1220 (cm^{-1})			
β-sheets	1222 - 1255	47	36	36	30	39	30
Random	1257 - 1281	18	18	19	19	20	20
Turns	1281 - 1302	15	20	23	28	20	29
α-helix	1302 - 1317	20	26	22	23	21	21

intermolecular forces between HSA and DA at C=O and C—N—H groups. This intermolecular interaction which is mainly due to collisions and weak interactions due to electrostatic forces between the HSA and DA causing unfolding of HSA to increase thus increasing the α-helix percentage. [15] [16] [34] [35]. It seems that the electrostatic forces between HSA and DA increase bonding in α-helix which is accompanied by decrease in β-sheets due to destabilization effects due to fast dynamic equilibrium which is consistent with the small binding constant value obtained from fluorescence in addition to weak hydrophobic contacts.

5. Discussion/Conclusions

In conclusion, the complexation of HSA-DA has been investigated using UV absorption spectroscopy, fluorescence spectroscopy, and FT-IR under physiological conditions. DA binds to HSA with binding constant of 4.4×10^2 and quenching constant of 1.32×10^9 L·mol^{-1}·s^{-1} at 25˚C.

The UV investigation repeatedly showed no complexation and a value for the binding constant was not determined due to the very weak interaction between DA and HSA when compared to added absorbance signals of individual absorbing HSA and DA. Fluorescence investigations indicate that the original fluorescence of HSA was quenched by DA through dynamic quenching mechanism which is consistent with the obtained value of quenching constants. Simply, DA must diffuse to HSA during the lifetime of the excited state. Once diffused and upon contact, Trp214 returns to its ground state. The small binding constant is in agreement with the quenching constant value.

There are several ways to distinguish between dynamic and static quenching. The first is to realize that upon complexation the newly formed complex usually has a different absorption spectrum from either of the complex components, therefore, changes on the absorption spectra are almost a diagnostic of a static quenching mechanism. The second hint usually is evident from the shape of the absorption spectra. Linear Stern-Volmer is almost always due to static quenching while non-linear is almost definitive criteria for either dynamic quenching due to purely collisional frequency or due to a mix of both static and dynamic quenching. Although dynamic and static processes are concurrently present in many systems, it is very important to realize the distinctive feature of the absorption spectra of such systems which result in an upward curvature which is not the case in HSA-DA system. Similar behavior in shape of the absorption spectra might be obtained in cases where there is more than one fluorophore accessible to the quencher *i.e.*, DA. In such cases, DA quenched Trp214 fluorophores on the surface but was not able to penetrate the hydrophobic interior of HSA due to hydrophobic forces from within the bulky HSA or the presence of charged quenchers such as the chloride ion of the dopamine hydrochloride and as a result DA would have limited surface intermolecular interaction due to inaccessibility of the interior Trp214 residue sites and only those residues on the

surface of the protein would be quenched. This is consistent with our findings in terms of fraction accessible for quenching of 5%. This behavior has been observed in protein fluorophore quenching by polar or charged quenchers. As a result, Stern-Volmer plots deviate from linearity toward the *x*-axis.

FT-IR spectra indicate increase in partial unfolding of the protein upon DA binding due to weak intermolecular hydrophobic electrostatic forces. The FT-IR results are consistent with fluorescence investigation.

The results reported in this paper are helpful to improve the understanding of the HSA interaction with DA. The biological significance of this investigation lies in the well-recognized role of HSA as a drug transporter to target specified organs in such a way that the target organ could be cured therefore it is very important to understand the various types of molecular interactions of HSA with drugs are essential in the drug delivery and in promotion alternative foundations for new pathways of drug delivery. DA is delivered using L-3,4-dihydroxyphenylalanine (L-DOPA), which is the precursor of DA, in treatment of Parkinson's disease due to lack of dopamine. We look forward to developing alternative ways to deliver DA more effectively instead of converting the precursor to dopamine. Now that we have such results indicating the quenched nature for fluorescence quenching, this could be the beginning to develop alternatives ways for enhancing the HSA-DA interactions enhancement to be able to deliver DA directly. Possible ways to achieve this goal could be by either derivatization of DA or by using nanoparticles functionalization.

Acknowledgements

This work is supported by the German Research Foundation DFG Grant No. DR228/24-2.

Conflicts of Interest

The authors declare no conflicts of interest regarding the publication of this paper.

References

[1] Dewick, P.M. (2006) Chapter 11 Essentials of Organic Chemistry: For Students of Pharmacy, Medicinal Chemistry and Biological Chemistry. 1st Edition, Wiley, Hoboken.

[2] Arias-Carrión, *et al.* (2010) Dopaminergic Reward System: A Short Integrative Review. *International Archives of Medicine*, **3**, 24-29. https://doi.org/10.1186/1755-7682-3-24

[3] Carlsson, A. (1959) The Occurrence, Distribution and Physiological Role of Catecholamines in the Nervous System. *Pharmacological Reviews*, **11**, 490-493.

[4] Narvaes, R. and Maria Martins de Almeida, R. (2014) Aggressive Behavior and Three Neurotransmitters: Dopamine, GABA, and Serotonin—A Review of the Last 10 Years. *Psychology & Neuroscience*, **7**, 601-607. https://doi.org/10.3922/j.psns.2014.4.20

[5] Olguín, H.J., Guzmán, D.C., García, E.H. and Mejía, G.B. (2016) The Role of Dopa-

mine and Its Dysfunction as a Consequence of Oxidative Stress. *Oxidative Medicine and Cellular Longevity*, **2016**, Article ID 9730467.

[6] Nobili, A. (2017) Dopamine Neuronal Loss Contributes to Memory and Reward Dysfunction in a Model of Alzheimer's Disease. *Nature Communications*, **8**, Article Number: 14727. https://doi.org/10.1038/ncomms14727

[7] Kähkönen, S., Ahveninen, J., Pekkonen, E., Kaakkola, S., Huttunen, J., *et al.* (2002) Dopamine Modulates Involuntary Attention Shifting and Reorienting: An Electromagnetic Study. *Clinical Neurophysiology*, **113**, 1894-1902. https://doi.org/10.1016/S1388-2457(02)00305-X

[8] Devos, D., Devedjian, J.-C. and Moreau, C. (2014) Is Dopamine Involved in Alzheimer's Disease? *Frontiers in Aging Neuroscince*, **6**, 1-6.

[9] Devos, D., Devedjian, J.-C. and Moreau, C. (2017) Intracerebroventricular Dopamine for Parkinson's Disease. *Oncotarget*, **8**, 45034-45035. https://doi.org/10.18632/oncotarget.17596

[10] Triarhou, L.C. (2000-2013) Dopamine and Parkinson's Disease. Madame Curie Bioscience Database, Landes Bioscience.

[11] Alexander, G.E. (2004) Biology of Parkinson's Disease: Pathogenesis and Pathophysiology of a Multisystem Neurodegenerative Disorder. *Dialogues in Clinical Neurosciences*, **6**, 259-280.

[12] Blanco, G. and ocnalB, A. (2017) Medical Biochemistry. 1 Edition, Academic Press, Cambridge, Massachusetts.

[13] Alekseev, R.J. and Rebane, A.L. (2012) Protein Biochemistry, Synthesis, Structure and Cellular Functions. Nova Science Pub Inc., UK ed. Edition.

[14] He, X.M. and Carter, D.C. (1992) Atomic Structure and Chemistry of Human Serum Albumin. *Nature*, **358**, 209-215. https://doi.org/10.1038/358209a0

[15] Fasano, M., Curry, S., Terreno, E., Galliano, M., Fanali, G., Narciso, P., Notari, S. and Ascenzi, P. (2005) The Extraordinary Ligand Binding Properties of Human Serum Albumin. *IUBMB Life*, **57**, 787-796. https://doi.org/10.1080/15216540500404093

[16] Yang, F., Zhang, Y. and Liang, H. (2014) Interactive Association of Drugs Binding to Human Serum Albumin. *International Journal of Molecular Sciences*, **15**, 3580-3595. https://doi.org/10.3390/ijms15033580

[17] Roy, S. (2016) Review on Interaction of Serum Albumin with Drug Molecules. *Research and Reviews: Journal of Pharmacology and Toxicological Studies*, **4**, 7-16.

[18] Larsen, *et al.* (2016) Albumin-Based Drug Delivery: Harnessing Nature to Cure Disease. *Molecular and Cellular Therapies*, **4**, 3-14. https://doi.org/10.1186/s40591-016-0048-8

[19] Yasseen, Z.J. and Ghossain, M.E. (2016) Studies on Binding of Widely Used Drugs with Human Serum Albumin at Different Temperatures and PHs. *iMedPub Journals*, **5**, 3.

[20] Korolev, I.O. (2014) Alzheimer's Disease: A Clinical and Basic Science Review. *Medical Student Research Journal*, **4**, 24-33.

[21] An, *et al.* (2008) Main Hypotheses, Concepts and Theories in the Study of Alzheimer's Disease. *Life Science Journal*, **5**, 1-5.

[22] Karch, C.M., Cruchaga, C. and Goate, A.M. (2014) Alzheimer's Disease Genetics: From the Bench to the Clinic. *Neuron*, **83**, 11-26. https://doi.org/10.1016/j.neuron.2014.05.041

[23] Lloyd, A., Demetrius, L.A., Magistretti, P.J. and Pellerin, L. (2015) Alzheimer's Disease: The Amyloid Hypothesis and the Inverse Warburg Effect. *Frontiers in Physiology*, **5**, 1-25.

[24] Rasheed, N. and Alghasham, A. (2012) Central Dopaminergic System and Its Implications in Stress-Mediated Neurological Disorders and Gastric Ulcers: Short Review. *Advances in Pharmacological Sciences*, **2012**, Article ID: 182671.

[25] Beitz, J.M. (2014) Parkinson's Disease: A Review. *Frontiers in Bioscience*, **6**, 65-74. https://doi.org/10.2741/S415

[26] Jankovic, J. (2008) Parkinson's Disease: Clinical Features and Diagnosis. *Journal of Neurology, Neurosurgery, and Psychiatry*, **79**, 368-376. https://doi.org/10.1136/jnnp.2007.131045

[27] Hoang, Q.Q. (2014) Pathway for Parkinson Disease. *PNAS*, **111**, 2402-2403. https://doi.org/10.1073/pnas.1324284111

[28] Burns, J.M., Galvin, J.E., Roe, C.M., Morris, J.C. and McKeel, D.W. (2005) The Pathology of the Substantia Nigra in Alzheimer Disease with Extrapyramidal Signs. *Neurology*, **64**, 1397-1403. https://doi.org/10.1212/01.WNL.0000158423.05224.7F

[29] Storga, D., Vrecko, K., Birkmayer, J.G. and Reibnegger, G. (1996) Monoaminergic Neurotransmitters, Their Precursors and Metabolites in Brains of Alzheimer Patients. *Neuroscience Letters*, **203**, 29-32. https://doi.org/10.1016/0304-3940(95)12256-7

[30] Selkoe, D.J. and Hardy, J. (2016) The Amyloid Hypothesis of Alzheimer's Disease at 25 Years. *EMBO Molecular Medicine*, **8**, 595-608. https://doi.org/10.15252/emmm.201606210

[31] Karran, E. and Hardy, J. (2014) Antiamyloid Therapy for Alzheimer's Disease—Are We on the Right Road? *The New England Journal of Medicine*, **370**, 377-378. https://doi.org/10.1056/NEJMe1313943

[32] Stansley, B.J. and Yamamoto, B.K. (2015) L-Dopa and Brain Serotonin System Dysfunction. *Toxics*, **3**, 75-88. https://doi.org/10.3390/toxics3010075

[33] Quinlan, G.J., Greg, S., Martin, G.S. and Evans, T.W. (2005) Albumin: Biochemical Properties and Therapeutic Potential. *Hepatology*, **41**, 1211-1219. https://doi.org/10.1002/hep.20720

[34] Zsila, F., Bikadi, Z., Malik, D., Hari, P., Pechan, I., Berces, A. and Hazai, E. (2011) Evaluation of Drug-Human Serum Albumin Binding Interactions with Support Vector Machine Aided Online Automated Docking. *Structural Bioinformatics*, **27**, 1806-1813.

[35] Lee, P. and Wu, X. (2015) Review: Modifications of Human Serum Albumin and Their Binding Effect. *Current Pharmaceutical Design*, **21**, 1862-1865. https://doi.org/10.2174/1381612821666150302115025

[36] Segura-Aguilar, J., *et al*. (2014) Protective and Toxic Roles of Dopamine in Parkinson's Disease. *Journal of Neurochemistry*, **129**, 898-915. https://doi.org/10.1111/jnc.12686

[37] Darwish, S.M., Aiaidah, S.Y., Khalid, I.M., Abuteir, M.M. and Qawasmi, L. (2015) Spectroscopic Investigations of β-Amyloid Interactions with Propofol and L-Arginine. *Open Journal of Biophysics*, **5**, 50-67. https://doi.org/10.4236/ojbiphy.2015.52005

[38] Darwish, S.M., Abu sharkh, S.E., Abuteir, M.M., Makharza, S.A. and Abu-hadid, M.M. (2010) Spectroscopic Investigations of Pentobarbital Interaction with Human Serum Albumin. *Journal of Molecular Structure*, **963**, 122-129. https://doi.org/10.1016/j.molstruc.2009.10.023

[39] Zheng, X., Li, Z., Podariu, M.I. and Hage, D.S. (2014) Determination of Rate Constants and Equilibrium Constants for Solution-Phase Drug-Protein Interactions by Ultrafast Affinity Extraction. *Analytical Chemistry*, **86**, 6454-6460. https://doi.org/10.1021/ac501031y

[40] Lakowicz, J.R. (1990) Principles of Fluorescence Spectroscopy. Kluwer Academic Publishers/Plenum Press, Dordrecht/New York, Chapter 8.

[41] Chen, G.Z., Huang, X.Z., Xu, J.G., Zheng, Z.Z. and Wang, Z.B. (1990) Method of Fluorescence Analysis. Science Press, Chapter 4.

[42] Topală, T., Bodoki, A., Oprean, L. and Radu, O. (2014) Experimental Techniques Employed in the Study of Metals Complexes-DNA Interactions. *Farmacia*, **62**, 1049-1061.

[43] Ivanov, A.I., Zhbankov, R.G., Korolenko, E.A., *et al*. (1994) Infrared and Raman Spectroscopic Studies of the Structure of Human Serum Albumin under Various Ligand Loads. *Journal of Applied Spectroscopy*, **60**, 305.

[44] Wu, Y., Czarnik-Matusewicz, B., Murayama, K. and Ozaki, Y. (2000) Two-Dimensional Near-Infrared Spectroscopy Study of Human Serum Albumin in Aqueous Solutions: Using Overtones and Combination Modes to Monitor Temperature-Dependent Changes in the Secondary Structure. *The Journal of Physical Chemistry B*, **104**, 5840-5847. https://doi.org/10.1021/jp000537z

[45] Dukor, R.K., Chalmers, J.M. and Griffiths, P.R. (2001) Vibrational Spectroscopy in the Detection of Cancer. In: *Handbook of Vibrational Spectroscopy*, Wiley, Hoboken, Vol. 5, Chapter 3.

[46] Krimm, S. and Bandekar, J. (1986) Vibrational Spectroscopy and Conformation of Peptides, Polypeptides, and Proteins. *Advances in Protein Chemistry*, **38**, 181-364. https://doi.org/10.1016/S0065-3233(08)60528-8

[47] Ahmed-Ouameur, A., Diamantoglou, S., Sedaghat-Herati, M.R., Nafisi, Sh., Carpentier, R. and Tajmir-Riahi, H.A. (2006) The Effects of Drug Complexation on the Stability and Conformation of Human Serum Albumin. *Cell Biochemistry and Biophysics*, **45**, 203-213. https://doi.org/10.1385/CBB:45:2:203

[48] Lee, P. and Wu, X. (2002) Interaction of Drugs with Bovine and Human Serum Albumin. *Journal of Molecular Structure*, **614**, 227-232. https://doi.org/10.1016/S0022-2860(02)00256-9

[49] Polavarapu, P.L. (1998) Vibrational Spectra: Principles and Applications with Emphasis on Optical Activity. Elsevier Science, Amsterdam, Vol. 85, Chapter 14.

[50] Garidel, P. and Schott, H. (2006) Fourier-Transform Midinfrared Spectroscopy for Analysis and Screening of Liquid Protein Formulations: Part 1, Understanding Infrared Spectroscopy of Proteins. *BioProcess International*, **4**, 40-46.

[51] Garidel, P. and Schott, H. (2006) Fourier-Transform Midinfrared Spectroscopy for Analysis and Screening of Liquid Protein Formulations Part 2: Detailed Analysis and Applications. *BioProcess International*, **4**, 48-55.

[52] Huang, X., Guo, X.-F., Wang, H. and Zhang, H.-S. (2014) Analysis of Catecholamines and Related Compounds in One Whole Metabolic Pathway with High Performance Liquid Chromatography Based on Derivatization. *Arabian Journal of Chemistry*. https://doi.org/10.1016/j.arabjc.2014.11.038

Scientific Research Publishing

Open Journal of Biophysics, 2019, 9, 131-145
http://www.scirp.org/journal/ojbiphy
ISSN Online: 2164-5396
ISSN Print: 2164-5388

The Intrinsic Self-Time of Biosystems

Oliver Szasz[1], Peter Gyula Szigeti[2], Andras Szasz[1]

[1]Department of Biotechnics, Szent Istvan University, Budapest, Gödöllő, Hungary
[2]Institute of Human Physiology and Clinical Experimental Research, Semmelweis University, Budapest, Hungary
Email: biotech@gek.szie

How to cite this paper: Szasz, O., Szigeti, P.G. and Szasz, A. (2019) The Intrinsic Self-Time of Biosystems. *Open Journal of Biophysics*, **9**, 131-145.
https://doi.org/10.4236/ojbiphy.2019.92010

Received: March 14, 2019
Accepted: April 6, 2019
Published: April 9, 2019

Abstract

In biological systems, self-time differs from the physical time scale. Biological self-time is the characteristic of individual biosystems and invariantly describes the various dynamic processes in organisms. This biological invariance is introduced by using 2 basic theorems: Allometric scaling and the Weibull psychometric function. Our objective was to precisely describe the timing phenomenon in biosystems and provide a framework to further develop this analogy for other fields.

Keywords

Psychometric Function, Allometry, Scaling, Bio-Invariance, Survival

1. Introduction

The lifetime of biological objects is measured by their dynamical development. Studies have a surprising universality by the self-organizing [1] [2] and consequently, self-similarity. A further consequence of this self-managed process is the spatiotemporal fractal structure [3] [4], and the bioscaling behavior, [5]. These ideas are forming the similarities of the species [6], which directly leads to an expected lifetime universality of well-selected cohorts. Heart rates are well scaled by the $\alpha = 1/4$ power-law by the body-mass in mammals [7] from the smallest to the largest. The allometry is generally applicable description from respiratory complexes, through the mitochondria, to the largest mass animals [8]. The heartbeat and the metabolic rate have the same mass-scaling dependence. The statistical value of the heart-beat in their lifetime does not change by the life-expectancy or by the mass of the organism and pretty stable for mammals around $n_{hb/lt} \approx (7.3 \pm 5.6) \times 10^8$ heartbeat/lifetime [9] which supports the unified delivery of the nutrition, but many other factors could modify this picture. Based on the universality, it is estimated, that all biological species have the

same basal oxygen consumption, ≈ 10^{-8} oxygen molecules per heartbeat [10]; this measurement defines the actual self-time. In consequence, the full lifetime (T_{lt}) is also scaled by the $\alpha = 1/4$ power-law, using the heartbeat (f_h) [9]:

$$T_{lt} = n_{hb/lt} / f_h \propto M^{1/4} \tag{1}$$

Self-time can be introduced on a thermodynamic optimizing basis when entropy production is constant over time [11]. Self-time is connected to allometry [12], and it scales with the allometric factor *a*. This power rule is strongly supported by various physiological times [13]. In a broader context, the intrinsic time could be explained similarly to the special relativity; time is not independent of space (only the space-time is invariant), and in biosystems, time is an integrative parameter of complex conditions [14].

Our objective is to study the self-time of biological objects in comparison to the coordinate time (clock time) measured by the observervations outside the studied bio-system, to develop an analogy for brittle materials by introducing the Weibull function (cumulative form of two-parametric Weibull distribution) for survival times. We transform time-scales and show the accuracy of the fit of Weibull based calculation to standard allometric scaling.

2. Weibull Statistics of Brittle Materials

The generalized cumulative Weibull distribution [15] is:

$$W(x) = \exp\left(-\left(\frac{x}{x_0}\right)^n\right), \tag{2}$$

where n is the shape factor, or form parameter, and x_0 is the scale parameter. This function is widely used in physiology and psychometry [16].

Weibull's statistics was originally developed to describe the fracture of brittle materials [15], and it provides the probability of a damage-free survival of a given material. The Weibull investigated brittle materials, such as ceramics, to describe the probability of breaks due to mechanical stress [15] [17]. Using the notation from [18], the "survival" of the material's integrity (P_S) and the survival rate probability define the percentage of sample breaks when multiple probes are tested. When processing the statistical data, the cumulative probability of survival at a homogeneous σ stress on a sample with V volume is:

$$P_S(\sigma, V) = \exp\left(-\frac{V}{V_0}\left(\frac{\sigma}{\sigma_0}\right)^n\right), \tag{3}$$

where V_0 is the reference volume, σ_0 is the reference stress, and n is the Weibull's form factor of the function. When experimenting with N samples, NP_S pieces of this count will not fail even under the maximum stress of σ. The reference stress and volume should be introduced into the exponent for dimensional reasons. When we have a sample where $V = V_0$ and $\sigma = \sigma_0$, and these are both independent from the form factor n, by solving the Equation (3) we obtain:

$$P_{S0} = \exp\left(-\frac{V_0}{V_0}\left(\frac{\sigma_0}{\sigma_0}\right)^n \right) \cong 0.3678. \tag{4}$$

Therefore, the survival probability of such a sample is 36.78%.

The above Weibull function (3) can be rewritten by using the familiar 2-parametric shape:

$$P_S(\sigma, V) = \exp\left(-V^{1/n}\left(\frac{V_0^{1/n}}{\sigma_0}\right)\left(\frac{\sigma}{x_0}\right)^n \right). \tag{5}$$

The relationship between the individual scale parameter characteristics can be readily associated with the Weibull statistics (2) used in the strength theory:

$$x = \sigma V^{1/n} \quad \text{and} \quad x_0 = \sigma_0 V_0^{1/n}. \tag{6}$$

It is possible to determine the survival probability of the same stress and volume relationship, *i.e.*, the scaling law from the Weibull distribution in (3), when we have the same survival probability:

$$\sigma = \frac{const}{V^{1/n}}, \tag{7}$$

which means a smaller sample is stronger and stabler than a larger one.

The Weibull function is based on 2 primary properties: volume dependence and self-similarity. To formulate the above equations in another way, imagine, that a sample is composed of 2 parts (**Figure 1**), and we want to express the likelihood of failure of the complete, complex system using the failure probability for each individual part.

By applying the Weibull Function (3) to the scenario shown in **Figure 1**, the likelihood of σ stress failure of the $V_1 + V_2$ sample volume is:

$$P_S(\sigma, V) = \exp\left(-\frac{V_1 + V_2}{V_0}\left(\frac{\sigma}{\sigma_0}\right)^n \right) = P_S(\sigma, V_1) P_S(\sigma, V_2). \tag{8}$$

From (7), sample failure occurs at the weakest location (the structural fault location). In the Weibull theory, the structural failure probability is proportional to the sample volume. The effect of the form factor is shown in **Figure 2**.

Step-function occurs at large form factors. In other words, if $\sigma \leq \sigma_0$, each sample component survives, however, when $\sigma > \sigma_0$, the entire sample fails. Materials composed of links with equal strength, that is, homogeneous chains like metals, show such behavior.

3. Links to Survival Characteristics of Patients

A recent study attempted to describe the connection between fractal geometry and the circulatory system with Weibull's survival function by using the age of the patient and body weight as its parameters [18]. Specifically, this study examined the link between brittle material fracture survival and cancer patient survival [18]. This allometric approach links geometric and life parameters

Figure 1. Two-part system for Weibull analysis.

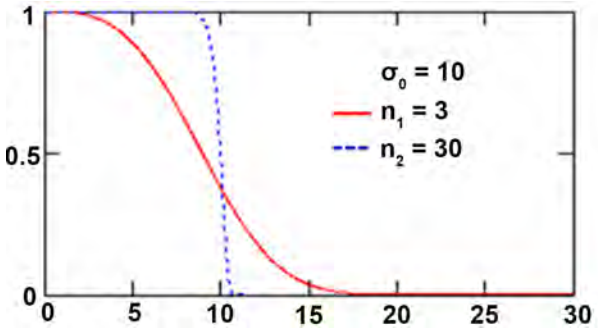

Figure 2. Form factor impact on the probability of survival.

(ontogenetic growth [19]), to survival probability described by the cumulative Weibull parametric distribution function [15]. The resulting function was used to assess the cancer patients' survival statistics. Since this approach utilized body mass, it did not examine the links between other patient details, including cancer type, vascularization or tumor size, on fractal geometry and actual survival statistics. Individuals are exposed to a variety of complex stresses—environmental, nutritional, physical, lifestyle-related and spiritual—that are not equivalent to the mechanical strength of inanimate material. There is no doubt, however, that in a cohort of healthy individuals with similar life stresses, the best single parameter may be their collected experiences.

The above assumption is not far from strength theory, where repetitive stress would likely be the best parameter to statistically investigate and characterize failure. This characterization is called the fatigue test. When each stress cycle takes a nearly identical course, the measurement can be reduced to a single parameter, and the load is characterized by the spending time. Statistical functions can describe both inanimate objects and organisms; although living organisms are far more complex than objects described with mechanical rheology. Indeed, we found many similarities between machine parts and the organs of a living body by using lifespan approximations with the Weibull function [15]. For example, one can compare machine part wear with the wear that results from mechanical friction and stress at joints. Both processes cause damage to the materials and influence lifespan. Additionally, heart diseases may be caused by increased electrical conductivity in specific heart regions that alters the initial sinus node electrical signal propagation and thus modifies heart function. Similarly, parts of a printed circuit board unit located in a wet and/or dusty environment would likely stop functioning appropriately. The actual size of the malfunctioning areas does not matter (as long as they are small), but over time the collective malfunctioning could cause failure, or disease in a biological system.

Malignant tumors are the result of altered biological activity in an organ. Tumor dynamism overloads normal systemic functions by their aggressive demands for nutrients and thus alters organ function. Hence, in addition to the tumor's metastasis, there are 3 direct reasons why organ failure may occur due to this malignant process:

- the cancerous metabolism overwhelms normal physiological consumption;
- tumor metabolism becomes comparable to the host organ metabolism;
- the geometric scale of the tumor makes normal organ function impossible.

Consequently, tumor size influences the individual's lifespan. Tumor volume is related to the structural failure probability. This parameter is constant over time for healthy individuals; however, the tumor size is time dependent. Therefore, there is a qualitative difference between the volumetric parameters of the Weibull law and the so-called "faulty volume" of the disease. Naturally, the growing cancerous tumor reduces survival probability. The increased, faulty tissue volume increases the probability of structural incompatibility problems and stress caused by the growing tumor increases the probability of failure. Thus, the analogy between mechanical failure and survival is as follows:

- mechanical stress, σ, is analogous to survival time t (or observation time during treatment);
- the reference stress, σ_0, is analogous to the scale parameter t_0 (the reference time in the therapy, when the survival probability is 36.8%);
- the volume, V, is analogous to the actual size (volume) or the actual metabolic activity (energy consumption rate) of the tumor, G(t). This function is additive and could be the volume or the metabolic rate. Both parameters are additive in the destructive process;
- the reference volume, V_0, is analogous with the reference size (volume) or the reference metabolic activity (energy consumption rate) of the tumor (G_0).

Hence, the Weibull law (as in (3) and (2)), which corresponds to survival by time (t) distribution is:

$$W(t) = \exp\left(-\left(\frac{t}{t_0}\right)^n\right); \tag{9}$$

alternatively, when considered in the context of an administered therapy, it is analogous with (3):

$$P_S(t) = \exp\left(-\frac{G(t)}{G_0}\left(\frac{t}{t_0}\right)^n\right). \tag{10}$$

4. Metabolic Considerations

As discussed above, tumor size could be geometric (volume) or metabolic (energy consumption). Extra energy demands are due to the high proliferative and metabolic processes of cancer cells. Indeed, tumor energy consumption may be several times higher than the metabolism of healthy cells, and energy is supplied by intensive glucose production from non-oxidative glycolysis [20].

The size of the host organism and its net metabolic rate (basal metabolic rate, R_0) can be expressed by the actual body mass (m) of the healthy adult individual, as introduced by the allometric considerations (allometric law [21]):

$$R_0 \propto m^{\alpha}. \tag{11}$$

In case of satisfactory nourishment, $\alpha = \alpha_0 = 3/4$ [22]. If one considers adult individuals, who would exhibit a stable mass (M), the mass-specific basal metabolic rate function would be:

$$\frac{R_0}{M} \propto M^{\alpha-1}. \tag{12}$$

These allometric considerations could be applied for organs, where M is the final, stable organ mass, and R_0 is the organ's basal metabolic rate.

Tumor growth satisfies the allometric metabolic rule; that exhibits universal growth dynamics [23] [24]. The approximate change in the number of tumor cells (n_c) depends on production (proliferation, P) and cell death (annihilation, A); A is proportional to n_c as shown below:

$$\frac{\mathrm{d}n_c}{\mathrm{d}t} = P - A \quad \text{and} \quad A = \lambda n_c, \tag{13}$$

where $\lambda^{-1} = T$ is the average life of the cell.

Energy balance has 3 components: energy to support current cells (the metabolic rate of a single cell, R_c), energy to produce new cells (E_c) and external work (W_e) on the system. All of these factors originate from the energy flux of blood flow (I) through capillary terminals:

$$I = R_c n_c + PE_c + W_e = R_c n_c + \left(\frac{\mathrm{d}n_c}{\mathrm{d}t} + \lambda n_c\right) E_c + W_e. \tag{14}$$

Due to allometric considerations [8] [19]:

$$I = R_0 n_c^{\alpha} \quad \text{and} \quad W_e = C_0 n_c^{\alpha}, \tag{15}$$

where $\alpha \le 1$ [25] [26]. Substitute these terms into (14):

$$E_c \frac{\mathrm{d}n_c}{\mathrm{d}t} = \left(R_0 - C_0\right) n_c^{\alpha} - n_c \left(R_c + \lambda E_c\right). \tag{16}$$

Multiply by the mass of an individual cell (m_c):

$$\frac{\mathrm{d}m}{\mathrm{d}t} = am^{\alpha} - bm \tag{17}$$

$$a = \frac{\left(R_0 - C_0\right) m_c^{(1-\alpha)}}{E_c}, \quad b = \frac{R_c}{E_c} + \lambda.$$

Due to energy flux changes by the α power of the mass during metabolism to maintain homeostasis, ($\mathrm{d}m/\mathrm{d}t$) is positive, and thus the maximum mass (M) is limited and can be expressed by the mass of a cell (m_c):

$$aM^{\alpha} - bM = 0 \rightarrow M = \left(\frac{a}{b}\right)^{\frac{1}{(1-\alpha)}} = \left(\frac{R_0 m_c^{(1-\alpha)}}{R_C + \lambda E_C}\right)^{\frac{1}{(1-\alpha)}} \tag{18}$$

When substituting b from (18) into (17), we get the Verhulst-Pearl differential equation [27], similar to the results of [18]:

$$\frac{\mathrm{d}m}{\mathrm{d}t} = am^{\alpha}\left(1-\left(\frac{m}{M}\right)^{(1-\alpha)}\right). \tag{19}$$

The solution of this differential equation describes a sigmoid curve:

$$\left(\frac{m}{M}\right)^{1-\alpha} = 1-\mathrm{e}^{-\tau}, \tag{20}$$

where

$$\tau = \frac{a(1-\alpha)t}{M^{(1-\alpha)}} - \ln\left(1-\left(\frac{m_0}{M}\right)^{(1-\alpha)}\right); \tag{21}$$

moreover, m_0 is the initial (birth) mass.

The ratio of energy flux for stationery stabilization and metabolism is:

$$r(t) = \frac{n_c R_c}{I} = \frac{mR_c}{m_c R_0 m^{\alpha}} = \frac{b}{a}m^{1-\alpha}. \tag{22}$$

Using (18) and (20), the relative metabolic rate for maintaining stationary equilibrium is:

$$r_m(t) = \left(\frac{m}{M}\right)^{1-\alpha} = 1-\mathrm{e}^{-\tau}; \tag{23}$$

moreover, the universal energy-function used for growth is:

$$R_m(t) = 1-r(t) = \mathrm{e}^{-\tau}. \tag{24}$$

$r(t)$ and $R(t)$ are the same functions of τ for all organs with m mass; the time-scale τ may be regarded as a biological self-time. τ is invariant for the organ or organism; it is a time scale that is determined wholly by the biological system and not by any outside processes. The existence of physiologic time, which is different from clock time, was previously hypothesized [28].

Equation (20) is a universal function, and so the above considerations are well suited to living organisms [8] [19] and tumor growth [23] [24], when self-time is defined as above. Maximum mass growth occurs at the inflection point, where:

$$\frac{\mathrm{d}^2 m}{\mathrm{d}t^2} = 0. \tag{25}$$

Here, mass and growth rate are:

$$m = \left(\frac{3}{4}\right)^4 M \cong \frac{M}{3}; \tag{26}$$

$$\frac{\mathrm{d}m}{\mathrm{d}t} = \frac{27a}{256}M^{2/3} \cong 0.1aM^{2/3},$$

when $\alpha = \alpha_0 = 3/4$. Thus, relative metabolic rate (r_m) and the part of metabolism related to growth ($R_m = 1-r_m$) are:

$$r_m = \frac{3}{4} \text{ and } R_m = \frac{1}{4}. \tag{27}$$

Several investigations have estimated that $2/3 \le \alpha \le 1$ depends on the fractal geometry of the nutrient supply of the tumor [25]. In the case of volumetric supply, $\alpha \approx 1$, while for surface supply, $\alpha \approx 2/3$ [29]. Consequently, it is necessary to examine the possibility of the above analogies with strength theory in the self-time (biological time) scale, τ (observation of biological self-time during therapy).

5. The Relationship between the Variants of Time Scales

Identical tumor size ($G(\tau) = G_0$) and biological self-time ($\tau = \tau_0$) could differ from the physical time (t) periods, and the survival probability (P_s) in this situation would be approximately 36.8%. However, the connection between the two-time scales, according to (20), is:

$$t = \frac{M^{(1-\alpha)}}{a(1-\alpha)}\left[\tau + \ln\left(1-\left(\frac{m_0}{M}\right)^{(1-\alpha)}\right)\right]. \tag{28}$$

The difference depends on the metabolic rate per unit volume, the initial size of the tumor and actual vascularization. Generally, scaling biological self-time shows the same survival probability of lifespan from (10) to any actual probability:

$$\frac{G(\tau)}{G_0}\left(\frac{\tau}{\tau_0}\right)^n \cong const. \tag{29}$$

Hence,

$$\tau \cong const\frac{\tau_0}{\left(\frac{G(\tau)}{G_0}\right)^{\frac{1}{n}}}. \tag{30}$$

Thus, survival time decreases as tumor size increases. The higher the value of m, the more it reduces the dependency rate. The physical timescale using (30) is:

$$t \cong const\frac{M^{(1-\alpha)}}{a(1-\alpha)}\left[\frac{\tau_0}{\left(\frac{G(\tau)}{G_0}\right)^{\frac{1}{n}}} + \ln\left(1-\left(\frac{m_0}{M}\right)^{(1-\alpha)}\right)\right]. \tag{31}$$

If we substitute (18) into (31) we get:

$$t \cong const\frac{1}{b(1-\alpha)}\left[\frac{\tau_0}{\left(\frac{G(\tau)}{G_0}\right)^{\frac{1}{n}}} + \ln\left(1-\left(\frac{m_0}{M}\right)^{(1-\alpha)}\right)\right]. \tag{32}$$

Consequently, if the enlarged initial mass decreases, the surface supply increases the physical lifetime. It is also clear from (32) that individuals with high-

er $G(\tau)$ would exhibit a reduced survival, especially when n is relatively small.

6. The Scaling Law and the Physical Timescale

From above, the Weibull law is applicable to biological self-time and also correlates with physical time. Lifespans connected to the same survival probability have a dependence as shown in (10) and similarly to (29):

$$\frac{G(\tau)}{G_0}\left(\frac{t}{t_0}\right)^n \cong const, \tag{33}$$

from which we conclude, that survival time decreases as tumor size increases:

$$t \cong const \frac{t_0}{\left(\frac{G(t)}{G_0}\right)^{\frac{1}{n}}}. \tag{34}$$

The greater the value of n, the more independent t is of G.

We know from [19] that the metabolic flux is:

$$\Phi = cm^{\alpha}, \tag{35}$$

where c is a constant with a peculiar dimension, that is, the nutrient flux per unit weight of the system. This is not a good measure since it is not additive. The additive rate is:

$$G(t) := \Phi^{\frac{1}{\alpha}} = c^{\frac{1}{\alpha}} m(t) \text{ and } G(\tau) := \Phi^{\frac{1}{\alpha}} = c^{\frac{1}{\alpha}} m(\tau); \tag{36}$$

alternatively, any of its homogeneous linear function.

From a mathematical point of view, 2 cases will produce a biparametric Weibull function:

$$G(\tau) \cong const = K \text{ or } G(\tau) \cong \tau^{\delta}. \tag{37}$$

The $G(\tau) \approx$ const case occurs when the tumor has almost reached its final size. This scenario may occur if tumor vascularization cannot sufficiently supply the required nutritional demand and/or due to interventional therapy. However, here $\alpha \approx 1$, denoting conformity with surrounding surface supply. This case is termed as a stagnant cancer. The second case is equivalent to the long physical time related to short biological time. This phenomenon could occur with a large M (matured tumor mass) or when the tumor supply is volumetric. τ could be $m_0 \approx 1$ and $\alpha \approx 1$; hence, the observed real-time survival would be accompanied with a very short biological self-time. This case represents a rapidly growing tumor.

When τ is small, the Equation (20) is well approximated by the linear function $1-e^{-\tau} \cong \tau$. Comparing this biological self-time scale set to the allometric law, the rate of weight is:

$$G(\tau) = m(\tau) = M\left(\left(\frac{m}{M}\right)^{1-\alpha}\right)^{\frac{1}{1-\alpha}} \cong M\tau^{\frac{1}{1-\alpha}}. \tag{38}$$

Substituting (37) for the Weibull function using the analogy of biological self-time, we get:

$$P_S = \exp\left(-\frac{M}{M_0}\left(\frac{\tau}{\tau_0^{n/q}}\right)^q\right) = \exp\left(-\left(\frac{\tau}{\tau_0^{n/q}\left(\frac{M}{M_0}\right)^{1/q}}\right)^q\right) \tag{39}$$

$$q = n + \frac{1}{1-\alpha},$$

where the selected reference is the metabolic flux of the tumor with the power α, and M_0 corresponds to the healthy reference G_0. If the tumor is near to the entirely surface-determined supply ($\alpha \approx 1$), the exponent will be large, the phenomenon will become digital (1 or 0, e.g., all or none) and the deviation of survival times will be low. The scaling law in this case would be:

$$\tau \cong const \cdot \tau_0^{1-\alpha}\left(\frac{M_0}{M}\right)^{\frac{1}{q}}. \tag{40}$$

This equation again shows that in the case of tumor surface feeding, survival time becomes independent of the parameters.

When the first condition of (37) is valid, then:

$$\tau \cong const \cdot \tau_0\left(\frac{M_0}{M}\right)^{\frac{1}{n}}. \tag{41}$$

When the second condition of (37) is valid (metabolic rate is high), then:

$$G(\tau) = a^{1/\alpha} m(\tau) = a^{1/\alpha} M\left(\left(\frac{m}{M}\right)^{1-\alpha}\right)^{\frac{1}{1-\alpha}} \cong a^{\frac{1}{\alpha}} M \tau^{\frac{1}{1-\alpha}}. \tag{42}$$

When we substitute (41) into the Weibull function obtained by using the biological self-time analogy, we get:

$$P_S = \exp\left(-\frac{a^{1/\alpha} M}{a_0^{4/3} M_0}\left(\frac{\tau}{\tau_0^{n/q}}\right)^q\right) = \exp\left(-\left(\frac{\tau}{\tau_0^{n/q}\left(\frac{a_0^{4/3} M_0}{a^{1/\alpha} M}\right)^{1/q}}\right)^q\right). \tag{43}$$

Concerning the metabolic flux of the reference tumor with allometric exponent α, we used $\alpha_0 = 3/4$ for the healthy (τ_0, reference) exponent.

It again appears that at a near surface supply condition, the exponent will be large and a digital behavior will occur. From this point of view, the scaling law is:

$$\tau \cong const \cdot \tau_0^{1-\alpha}\left(\frac{a_0^{\frac{4}{3}} M_0}{a^{\frac{1}{\alpha}} M}\right)^{\frac{1}{q}} \tag{44}$$

Again, the above equation describes universal behavior, namely, that survival time increasingly becomes independent in the case of surface supply. According to the second equation of (42), a simple deduction to the real physical time scale from the above equation to describe biological self-time leads to:

$$\tau \cong \frac{a(1-\alpha)t}{M^{1-\alpha}} = b(1-\alpha)t. \tag{45}$$

Substituting (44) into (43), we get the Weibull law associated with the physical time scale:

$$P_S = \exp\left(-\frac{a^{1/\alpha}M}{a_0^{4/3}M_0}\left(\frac{\tau}{\tau_0^{1-\alpha}}\right)^q\right) = \exp\left(-\left(\frac{t}{\frac{\tau_0^{1-\alpha}}{b(1-\alpha)}\left(\frac{a_0^{4/3}M_0}{a^{1/\alpha}M}\right)^{1/q}}\right)^q\right). \tag{46}$$

Consequently:

$$t \cong const \cdot \frac{\tau_0^{1-\alpha}}{b(1-\alpha)}\left(\frac{a_0^{\frac{4}{3}}M_0}{a^{\frac{1}{\alpha}}M}\right)^{\frac{1}{q}}. \tag{47}$$

We again see that the supply tends to become localized at the surface when $\alpha \to 1$, and so the growth of the tumor becomes independent of the survival parameters.

7. Allometry Scaling and Weibull Function

Several theories describe the growth of cell populations (including tumors). The time dependence of tumor size has several competing theories, but recently hyperbolic growth models have been proposed [30]. Weibull's law provides a simplified version of the general hyperbolic fit. The tumor size (e.g., the mass) satisfies the following equation in the hyperbolic model:

$$\frac{\mathrm{d}\left(\frac{m}{M}\right)}{\mathrm{d}t} = \left(1-\frac{m}{M}\right)\frac{\lambda}{\beta^\lambda}t^{\lambda-1}, \tag{48}$$

where M is the final tumor size. This equation is actually the Weibull equation. The solution is:

$$\frac{m}{M} = 1-\left(1-\frac{m}{M}\right)\exp\left(-\left(\frac{t}{\beta}\right)^\lambda\right); \tag{49}$$

or slightly modified:

$$\frac{m}{M} = 1-\mathrm{e}^{-\tau}; \tag{50}$$

$$\tau := \left(\frac{t}{\beta}\right)^\lambda - \ln\left(1-\frac{m_0}{M}\right).$$

If $m_0 \ll M$, then:

$$\frac{m}{M} = 1 - \mathrm{e}^{-\left(\frac{t}{\beta}\right)^{\lambda}}, \tag{51}$$

and the equation is returned to the well-known Weibull law. Considering (20), the allometric law could be formulated as:

$$\frac{m}{M} = \left(1 - \mathrm{e}^{-\tau}\right)^{1/(1-\alpha)}. \tag{52}$$

A simple comparison shows the validity of the approximation of the allometric law using the Weibull's function (Figure 3).

The Shannon entropy of the Weibull functions for fits to $\alpha = \frac{2}{3}$ and $\alpha = \frac{3}{4}$ are $s_{2/3} \cong 1.403$, and $s_{2/3} \cong 1.452$; respectively. This ≅ 3.5% difference shows a more certain death (less lifetime) in the $\alpha = \frac{2}{3}$ case than in $\alpha = \frac{3}{4}$, because the growing entropy shows a growing uncertainty.

This observation reveals a more profound relationship and can be proven by rigorous mathematical calculation. If α and β are large values in (50), then the following linear approximation is valid:

$$\frac{m}{M} \approx \left(\frac{t}{\beta}\right)^{\lambda}. \tag{53}$$

Thus, rapidly growing tumors could also be described by the Weibull evolutive equation. Note, that the probability of cumulative survival covariates with the normalized tumor size, *i.e.*:

$$\frac{m}{M} = 1 - \mathrm{e}^{-\left(\frac{t}{\beta}\right)^{\lambda}} \cong F_S(t). \tag{54}$$

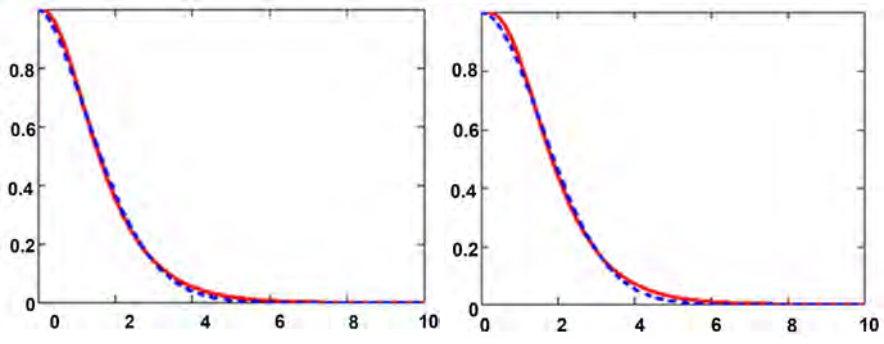

(a) (b)

Figure 3. The allometric law (solid line) of survival could be well approximated by the Weibull function (dashed line). (a) $\alpha = \frac{2}{3}; n \cong 1.698, t_0 \cong 2.005; error < 2 \times 10^{-3}$ (b) $\alpha = \frac{3}{4}; n \cong 1.917, t_0 \cong 2.286; error < 2 \times 10^{-3}$. (The error is defined by the integral of the square of the differences of the functions in the [0, 10] interval.)

The same can also be formulated in a more approximate version. The cumulative survival probability is the self-similar function of $(1 - m/M)$. In other words, the slopes of Equations (55) and (56) are equal, and the straight lines are parallel.

$$\ln(t) \mapsto \ln\left(\ln\left(F_S(t)\right)\right); \tag{55}$$

$$\ln(t) \mapsto -\ln\left(\ln\left(1-\frac{m}{M}\right)\right). \tag{56}$$

This formulation allows the fitting of the β scale parameter of survival to the final mass of the tumor (or to fit other tumor characteristics). In other words, $\ln\left(F_S(t)\right)$ is a self-similar function of $\ln(1 - m/M)$, so:

$$\ln\left(\ln\left(F_S(t)\right)\right) = K_1 \ln(K_2) \ln\left(1-\frac{m}{M}\right), \tag{57}$$

where K_1 and K_2 are constants.

8. Conclusion

We proposed an intrinsic time model that differs from clock time. We analyzed the self-time for tumor growth and showed its scaling based on allometric scaling as well as compared it to the Weibull physiologic function. The allometric function could be well approached by the Weibull function which highlights the intrinsic values of both the bioscaling and the Weibull physiologic function for living objects.

Acknowledgements

This research was supported by a Hungarian Competitiveness and Excellence Program grant (NVKP_16-1-2016-0042).

Conflicts of Interest

The authors declare no conflicts of interest regarding the publication of this paper.

References

[1] Walleczek, J. (2000) Self-Organized Biological Dynamics and Nonlinear Control. Cambridge University Press, Cambridge.

[2] Camazine, S., Deneubourg, J.L., Franks, N.R., *et al.* (2003) Self-Organization in Biological Systems (Princeton Studies in Complexity). Princeton University Press, Princeton, Oxford.

[3] Bassingthwaighte, J.B., Leibovitch, L.S. and West, B.J. (1994) Fractal Physiology. Oxford University Press, New York, Oxford.

[4] Kurakin, A. (2011) The Self-Organizing Fractal Theory as a Universal Discovery Method: The Phenomenon of Life. *Theoretical Biology and Medical Modelling*, **8**, Article ID: 23008. https://doi.org/10.1186/1742-4682-8-4

[5] Glazier, D.S. (2014) Metabolic Scaling in Complex Living Systems. *Systems*, **2**, 451-540.

[6] Scheffer, M. and van Nes, E.H. (2006) Self-Organized Similarity, the Evolutionary

Emergence of Groups of Similar Species. *Proceedings of the National Academy of Sciences of the United States of America*, **103**, 6230-6235. https://doi.org/10.1073/pnas.0508024103

[7] Savage, V.M., Gillooly, J.F., Woodruff, W.H., *et al.* (2004) The Predominance of Quarter-Power Scaling in Biology. *Functional Ecology*, **18**, 257-282. https://doi.org/10.1111/j.0269-8463.2004.00856.x

[8] West, G.B., Woodruf, W.H. and Born, J.H. (2002) Allometric Scaling of Metabolic Rate from Molecules and Mitochondria to Cells and Mammals. *Proceedings of the National Academy of Sciences of the United States of America*, **99**, 2473-2478. https://doi.org/10.1073/pnas.012579799

[9] Levine, H.J. (1997) Rest Heart Rate and Life Expectancy. *Journal of the American College of Cardiology*, **30**, 1104-1106.

[10] Azbel, M.Y. (1994) Universal Biological Scaling and Mortality. *Proceedings of the National Academy of Sciences of the United States of America*, **91**, 12453-12457. https://doi.org/10.1073/pnas.91.26.12453

[11] Andresen, B., Shiner, J.S. and Uehlinger, D.E. (2002) Allometric Scaling and Maximum Efficiency in Physiological Eigen Time. *Proceedings of the National Academy of Sciences of the United States of America*, **99**, 5822-5824. https://doi.org/10.1073/pnas.082633699

[12] Brown, J.H. and West, G.B. (2000) Scaling in Biology. Oxford University Press, Oxford.

[13] Gunther, B. and Morgado, E. (2005) Allometric Scaling of Biological Rhythms in Mammals. *Biological Research*, **38**, 207-212. https://doi.org/10.4067/S0716-97602005000200010

[14] Smith, J.D.H. (2003) Time in Biology and Physics. In: Buccheri, R., Saniga, M., Stuckey, W.M., Eds., *The Nature of Time*: *Geometry*, *Physics and Perception*, Springer, Dordrecht, 145-122. https://doi.org/10.1007/978-94-010-0155-7_15

[15] Weibull, W. (1951) A Statistical Distribution Function of Wide Applicability. *Journal of Applied Mechanics*, **18**, 293-297.

[16] Klein, S.A. (2001) Measuring, Estimating, and Understanding the Psychometric Function: A Commentary. *Perception and Psychophysics*, **63**, 1421-1455. https://doi.org/10.3758/BF03194552

[17] Weibull, W. (1939) The Statistical Theory of the Strength of Materials. Ph.D. Thesis, Royal Technical University, Stockholm.

[18] Pugno, N.M. (2005) On the Statistical Law of Life. Quant. Biol. Pop. Ecol.

[19] West, G.B., Brown, J.H. and Enquist, B.J. (2001) A General Model for Ontogenetic Growth. *Nature*, **413**, 628-631. https://doi.org/10.1038/35098076

[20] Hsu, P.P. and Sabatini, D.M. (2008) Cancer Cell Metabolism: Warburg and Beyond. *Cell*, **134**, 703-707. https://doi.org/10.1016/j.cell.2008.08.021

[21] Brown, J.H., West, G.B. and Enquis, B.J. (2005) Yes, West, Brown and Enquist's Model of Allometric Scaling Is Both Mathematically Correct and Biologically Relevant. *Functional Ecology*, **19**, 735-738. https://doi.org/10.1111/j.1365-2435.2005.01022.x

[22] West, G.B., Brown, J.H. and Enquist, B.J. (1999) The Fourth Dimension of Life: Fractal Geometry and Allometric Scaling of Organisms. *Science*, **284**, 1677-1679. https://doi.org/10.1126/science.284.5420.1677

[23] Guiot, C., Degiorgis, P.G., Delsanto, P.P., Gabriele, P. and Deisboeck, T.S. (2003) Does Tumor Growth Follow a "Universal Law"? *Journal of Theoretical Biology*,

225, 147-151.

[24] Bru, A., Albertos, S., Subiza, J.L., García-Asenjo, J.L. and Bru, I. (2003) The Universal Dynamics of Tumor Growth. *Biophysical Journal*, **85**, 2948-2961. https://doi.org/10.1016/S0006-3495(03)74715-8

[25] Szasz, O., Vincze, Gy., Vancsik, T. and Szigeti, Gy. (2017) Metabolic Rate of Cancer Clusters. *BMC Theoretical Biology and Medical Modelling*, Submitted.

[26] West, G.B. and Brown, J.H. (2005) The Origin of Allometric Scaling Laws in Biology from Genomes to Ecosystems: Towards a Quantitative Unifying Theory of Biological Structure and Organization. *Journal of Experimental Biology*, **208**, 1575-1592. https://doi.org/10.1242/jeb.01589

[27] Sunday, J., James, A.A., Ibijola, E.A., Ogunrinde, R.B. and Ogunyebi, S.N. (2012) A Computational Approach to Verhulst-Pearl Model. *IOSR Journal of Mathematics*, **4**, 6-13. https://doi.org/10.9790/5728-0430613

[28] West, D. and West, B.J. (2013) Physiologic Time: A Hypothesis. *Physics of Life Reviews*, **10**, 210-224. https://doi.org/10.1016/j.plrev.2013.04.006

[29] Carpinteri, A. and Pugno, N. (2002) One, Two, and Three-Dimensional Universal Laws for Fragmentation Due to Impact and Explosion. *Journal of Applied Mechanics*, **69**, 854-856. https://doi.org/10.1115/1.1488937

[30] Tabatabai, M., Williams, D.K. and Bursac, Z. (2005) Hyperbolastic Growth Models: Theory and Application. *Theoretical Biology and Medical Modelling*, **2**, Article ID: 21221. https://doi.org/10.1186/1742-4682-2-14

Call for Papers

Open Journal of Biophysics

ISSN Print: 2164-5388 ISSN Online: 2164-5396
http://www.scirp.org/journal/ojbiphy

Open Journal of Biophysics (OJBIPHY) is an international journal dedicated to the latest advancement of biophysics. The goal of this journal is to provide a platform for scientists and academicians all over the world to promote, share, and discuss various new issues and developments in different areas of biophysics.

Subject Coverage

All manuscripts must be prepared in English, and are subject to a rigorous and fair peer-review process. Accepted papers will immediately appear online followed by printed hard copy. The journal publishes original papers including but not limited to the following fields:

- Bioelectromagnetics
- Bioenergetics
- Bioinformatics and Computational Biophysics
- Biological Imaging
- Biomedical Imaging and Bioengineering
- Biophysics of Disease
- Biophysics of Photosynthesis
- Cardiovascular Biophysics
- Cell Biophysics
- Medical Biophysics
- Membrane Biophysics
- Molecular Biophysics and Structural Biology
- Physical Methods
- Physiology and Biophysics of the Inner Ear
- Proteins and Nucleic Acids Biophysics
- Radiobiology
- Receptors and Ionic Channels Biophysics
- Sensory Biophysics and Neurophysiology
- Systems Biophysics
- Theoretical and Mathematical Biophysics

We are also interested in: 1) Short Reports—2-5 page papers where an author can either present an idea with theoretical background but has not yet completed the research needed for a complete paper or preliminary data; 2) Book Reviews—Comments and critiques.

Notes for Intending Authors

Submitted papers should not have been previously published nor be currently under consideration for publication elsewhere. Paper submission will be handled electronically through the website. All papers are refereed through a peer review process. For more details about the submissions, please access the website.

Website and E-Mail

http://www.scirp.org/journal/ojbiphy E-mail: ojbiphy@scirp.org

What is SCIRP?

Scientific Research Publishing (SCIRP) is one of the largest Open Access journal publishers. It is currently publishing more than 200 open access, online, peer-reviewed journals covering a wide range of academic disciplines. SCIRP serves the worldwide academic communities and contributes to the progress and application of science with its publication.

What is Open Access?

All original research papers published by SCIRP are made freely and permanently accessible online immediately upon publication. To be able to provide open access journals, SCIRP defrays operation costs from authors and subscription charges only for its printed version. Open access publishing allows an immediate, worldwide, barrier-free, open access to the full text of research papers, which is in the best interests of the scientific community.

- High visibility for maximum global exposure with open access publishing model
- Rigorous peer review of research papers
- Prompt faster publication with less cost
- Guaranteed targeted, multidisciplinary audience

Scientific Research Publishing

Website: http://www.scirp.org

Subscription: sub@scirp.org

Advertisement: service@scirp.org